

Interferon Regulatory Factor 5 represses oxidative respiration in human and murine macrophages by inhibition of mitochondrial matrix protein GHITM

Lucie Oriaguet

Centre de Recherche des Cordeliers, INSERM, IMMEDIAB Laboratory, Sorbonne Université, Université de Paris <https://orcid.org/0000-0002-3209-457X>

Tina Ejlalmanesh

Centre de Recherche des Cordeliers, INSERM, IMMEDIAB Laboratory, Sorbonne Université, Université de Paris

Alexandre Humbert

CarMeN Laboratory, INSERM UMR-1060, Lyon 1 University, INRA U1397, F-69921,

Raphaëlle Ballaire

Inovarion

Marc Diedisheim

Centre de Recherche des Cordeliers, INSERM, IMMEDIAB Laboratory, Sorbonne Université, Université de Paris

Jean-Baptiste Julla

Centre de Recherche des Cordeliers, INSERM, IMMEDIAB Laboratory, Sorbonne Université, Université de Paris

Jessica Michieletto

Université Paris-Saclay, CEA, INRAE, Département Médicaments et Technologies pour la Santé (DMTS), MetaboHUB, F-91191

Judith Charbit

Centre Hospitalier Territorial Gaston-Bourret, Noumea, New Caledonia

Daniel Linden

AstraZeneca (Sweden)

Jeremie Boucher

AstraZeneca (Sweden)

Charline Potier

Centre de Recherche des Cordeliers, INSERM, IMMEDIAB Laboratory, Sorbonne Université, Université de Paris

Akila Hamimi

Centre de Recherche des Cordeliers, INSERM, IMMEDIAB Laboratory, Sorbonne Université, Université de Paris

Sophie Lemoine

Genomics core facility, Institut de Biologie de l'ENS (IBENS), Département de biologie, École normale supérieure, CNRS, INSERM, Université PSL, 75005 Paris, France <https://orcid.org/0000-0003-0975-5365>

Corinne Blugeon

Genomics core facility, Institut de Biologie de l'ENS (IBENS), Département de biologie, École normale supérieure, CNRS, INSERM, Université PSL, 75005 Paris, France

Patricia Legoix

Institut Curie Genomics of Excellence Platform, Institut Curie Research Center, PSL University, Paris, France

Sonia Lameiras

Institut Curie Genomics of Excellence Platform, Institut Curie Research Center, PSL University, Paris, France

Laura Baudrin

Institut Curie Genomics of Excellence Platform, Institut Curie Research Center, PSL University, Paris, France

Sylvain Baulande

Institut Curie Genomics of Excellence Platform, Institut Curie Research Center, PSL University, Paris, France <https://orcid.org/0000-0003-3104-1684>

Antoine Soprani

Centre de Recherche des Cordeliers, Inserm, University of Paris, IMMEDIAB Laboratory, F-75006, Paris, France; Department of Digestive Surgery, Générale de Santé (GDS), Geoffroy

Florence Castelli

Service de Pharmacologie et Immuno-Analyse (SPI), Laboratoire d'Etude du Métabolisme des Médicaments, CEA, INRA, Université Paris Saclay, Metabo HUB, F-91191, Gif-sur-Yvette

Francois Fenaille

Atomic Energy and Alternative Energies Commission

Jean-Pierre Riveline

Centre de Recherche des Cordeliers, INSERM, IMMEDIAB Laboratory, Sorbonne Université, Université de Paris

Jennifer Rieusset

Univ-Lyon, CarMeN Laboratory, INSERM 1060, INRA 1397, Université Claude Bernard Lyon1, INSA Lyon, Oullins, France. IHU OPERA, Groupement Hospitalier EST, Bâtiment B13, 59 boulevard Pinel

Jean-François Gautier

Centre de Recherche des Cordeliers, INSERM, IMMEDIAB Laboratory, Sorbonne Université, Université de Paris

Nicolas Venteclef

CRC Des Cordeliers

Fawaz Alzaid (✉ fawaz.alzaid@gmail.com)

Centre de Recherche des Cordeliers, INSERM, IMMEDIAB Laboratory, Sorbonne Université, Université de Paris <https://orcid.org/0000-0003-3056-3640>

Article

Keywords: diet-induced obesity (DIO), adipose tissue macrophage (ATM), Interferon Regulatory Factor 5

Posted Date: May 6th, 2021

DOI: <https://doi.org/10.21203/rs.3.rs-477956/v1>

License:   This work is licensed under a Creative Commons Attribution 4.0 International License.

[Read Full License](#)

Version of Record: A version of this preprint was published at Nature Communications on August 30th, 2022. See the published version at <https://doi.org/10.1038/s41467-022-32813-z>.

Abstract

Over the course of diet-induced obesity (DIO), adipose tissue macrophage (ATM) populations transition from highly oxidative and protective to highly inflammatory and metabolically deleterious. Here, we demonstrate that the Interferon Regulatory Factor (IRF)-5 is a key molecular switch mediating repression of macrophage oxidative capacity early in DIO. ATMs from mice with a myeloid-specific deletion of IRF5 are characterised by increased mitochondrial activity and oxidative respiration compared to ATMs from wild-type mice. This hyper-oxidative phenotype is inducible and reversible *in vitro* by delivery of an inhibitory IRF5-decoy peptide and through IRF5 adenoviral over-expression, respectively. In a data-driven approach, using public IRF5-cistrome data and in-house RNA-sequencing, we identified a transcriptional mechanism by which cellular oxidative capacity is repressed in an IRF5-dependent manner. The hyper-oxidative phenotype of IRF5-deficient macrophages is mediated by the Growth Hormone Inducible Transmembrane Protein (GHITM), known for maintaining mitochondrial architecture for optimal oxidative respiration. Cas9-mediated simultaneous knock-down of GHITM and of IRF5 reverses the hyper-oxidative phenotype associated with IRF5-deficiency *in vitro*. IRF5-dependent regulation of GHITM expression and mitochondrial activity extends to human ATMs and monocytes from obese and diabetic patients.

Introduction

ATMs are a heterogeneous population of cells with a range of beneficial and deleterious functions¹⁻⁶. Lipid associated macrophages (LAMs) have been reported to be a key beneficial ATM population, with a high capacity to clear dead and dying adipocytes as well as lipid droplets¹, while metabolically activated macrophages (MMe) exhibit both beneficial and harmful functions². A recent report by Sárvári *et al.* has also identified 6 distinct subpopulations of ATMs through snRNA-seq, of which two LAM subpopulations were characterised⁵. Predominance of each of these ATM populations is extremely time-dependent. ATMs physiologically attempt to maintain homeostasis in early caloric excess and over time, they become increasingly inflammatory, contributing to systemic inflammation and worsening insulin resistance. Inflammatory ATMs are critical actors in the development of type-2 diabetes (T2D) and other manifestations of metabolic syndrome.

Macrophage cellular metabolism is a major mitigating or optimising factor of immune effector functions^{7,8}. Pro-inflammatory functions are dependent on glycolysis, transcriptionally mediated by hypoxia inducible factor (HIF)-1 α , and targeted interruptions of the mitochondrial tricarboxylic acid (TCA) cycle. Conversely, anti-inflammatory polarisation or resolution is supported by mitochondrial respiration and oxidative metabolism. The hallmark investigations that brought these mechanisms to light were carried out in model systems of macrophages applying canonical stimulants of polarisation. More recent studies found that, in addition to canonical stimuli, microenvironmental niches also dictate energetic responses of immune cells. For example, highly active mitochondrial respiration gives regulatory T-cells a metabolic advantage over other immune cells in low-glucose high-lactate environments⁹.

In the context of metabolic syndrome, cells of the immune system are exposed to the same dysmetabolism as all peripheral tissues, that is glucolipotoxicity which represents a systemic abundance of metabolic substrates. In diet-induced obesity, ATMs are now known to have their own adaptive metabolism. They exhibit a hypermetabolic phenotype with excessive glycolytic and oxidative fluxes compared to lean physiological circumstances¹⁰⁻¹⁵. These important findings indicate that as sentinel cells, macrophages are reactive beyond inflammatory polarisation and their successful early metabolic adaptation may mitigate inflammatory polarisation and systemic metabolic decline.

Our previous work identified the Interferon Regulatory Factor (IRF)-5 as a key molecular switch mediating M1-like polarisation of ATMs¹⁶. We demonstrated that chronic high-fat feeding increases IRF5 expression in ATMs, in turn promoting pro-inflammatory polarisation and the transcriptional repression of TGF β signalling. This results in maladaptive white adipose tissue (WAT) expansion and systemic metabolic decline. Physiologically, IRF5 promotes transcription of pro-inflammatory cytokines and chemokines in macrophages in response to bacterial and viral stimuli¹⁷⁻¹⁹. Several lines of evidence implicate deregulated IRF5 expression in conditions of chronic inflammation, including auto-immune and metabolic diseases²⁰⁻²³. Notably, gain-of-function IRF5 risk-variants are associated with a multitude of auto-immune diseases and, more recently, with promoting macrophage glycolytic programming in auto-immunity (systemic lupus, irritable bowel disease, rheumatoid arthritis)^{16,24,25}. In-line with these reports, we hypothesised that IRF5 may also orient ATM metabolism, notably by repressing oxidative respiration that supports protective macrophage phenotypes predominant in early caloric excess.

Here, we reveal a non-canonical function of IRF5 in orienting bioenergetic adaptation of ATMs early in the course of diet-induced obesity. Upon short-term caloric excess we demonstrate that IRF5 restricts the cellular lipid pool and downregulates expression of components required to maintain efficient mitochondrial oxidative respiration. Through downregulation of the *Growth Hormone Inducible Transmembrane protein* (GHITM), also known as *Mitochondrial Morphology and Cristae Structure 1* (MICS1), IRF5 contributes to failure in maintaining normal inner membrane architecture required for effective oxidative respiration. Furthermore, the IRF5-GHITM axis of cellular bioenergetic adaptation extends to circulating monocytes and ATMs in diabetic and obese humans.

Results

Caloric excess is associated with ATM metabolic adaptation and increased IRF5 expression

To evaluate metabolic adaptation in ATMs, we placed C57BL/6J mice on a high-fat or normal chow diet (HFD, NCD) for 4 weeks, and quantified IRF5 expression and metabolic markers in epididymal WAT (EpiWAT) ATMs. As expected, mice on HFD gained more weight than mice on NCD over the 4 weeks, increasing WAT mass (Fig. S1A) and losing systemic insulin sensitivity and glucose tolerance (Fig. S1B). In EpiWAT, we found increased expression of F4/80 and MCP1 indicating increased macrophage recruitment, and increased expression of IRF5 (Fig. S1C). We carried out cytometric analyses in the EpiWAT stromal vascular fraction (SVF) and confirmed an increase in F4/80⁺CD11b⁺ macrophage

numbers, also histologically indicated by the presence of crown-like structures following HFD (Fig. 1A). In F4/80⁺CD11b⁺ cells, we confirmed an increase in IRF5 expression and M1-like marker CD11c expression, with no difference in M2-like marker CD206 (Fig. 1B). Assessing metabolic substrates, we used BODIPY, a fluorescent lipid dye, and 2-NBDG to assess glucose uptake. Upon short-term HFD, ATMs have increased intracellular lipids and increased glucose uptake relative to mice on NCD (Fig. 1C), as previously reported on longer term HFD¹¹. Next, we analysed mitochondrial mass and activity with the fluorescent JC-1 dye which is sensitive to mitochondrial membrane potential²⁶. We found trends to increased mitochondrial mass, decreased activity and decreased activity-to-mass ratio in ATMs from mice on HFD (Fig. S1D). Correlative analyses revealed that EpiWAT ATM numbers positively correlated to IRF5 expression in ATMs (Fig. 1D). Macrophage glucose uptake and mitochondrial mass positively correlated to IRF5 expression, whereas activity-to-mass ratio was negatively correlated to IRF5 expression (Fig. 1E). As macrophage numbers and IRF5 expression were positively correlated, IRF5 may disproportionately impact infiltrating macrophages. We analysed F4/80^{Hi} ATMs, previously characterised as monocyte-derived infiltrating macrophages^{10,27}, and found that F4/80^{Hi} ATMs had higher expression of IRF5 on HFD relative to NCD, with increased lipid content and glucose uptake (Fig. 1F, S1E). Interestingly, F4/80^{Hi} ATMs also had increased mitochondrial mass and decreased mitochondrial activity upon HFD relative to NCD (Fig. 1G). These data suggest that IRF5 plays a role in driving ATM infiltration and metabolic adaptation, including alterations in mitochondrial mass or activity on short-term HFD.

Myeloid-deficiency of IRF5 alters ATM metabolic adaptation to caloric excess

To discern whether ATM metabolic adaptation associated with IRF5 expression are dependent on IRF5, we applied the same model of short-term high-fat feeding to mice with a myeloid-deficiency of IRF5 (IRF5-KO) and their wild-type (WT) littermates (Fig. 1H). Despite no difference in systemic glucose homeostasis, body weight nor adipose tissue weight, we observed increased mitochondrial activity and activity-to-mass ratio in ATMs from IRF5-KO relative to WT mice (Fig. 1I, S1G). This was accompanied by a trend to increased lipid content in IRF5-KO but no difference in CD11c expression nor in glucose uptake (Fig. 1J). Unsupervised tSNE analyses confirmed that JC1-red fluorescence, indicating mitochondrial activity, was highest in F4/80^{Hi} ATMs and that these ATMs had higher fluorescence in IRF5-KO (Fig. 1K). To determine whether these effects on macrophage metabolism are reflected at the transcriptomic level or are time-dependent, we sorted F4/80⁺ cells from epididymal fat pads of IRF5-KO and WT mice upon HFD for 4 and 12 weeks. Differential analyses between genotypes and GO term enrichment revealed that terms related to cellular metabolism were over-enriched, whilst those related to immune effector functions were under-enriched at 4 weeks, comforting our *in vivo* and cellular results showing that metabolic pathways are altered in an IRF5-dependent manner at 4 weeks of HFD (Fig. 1L). On long-term HFD, we previously reported that IRF5-deficiency results in a protected systemic metabolic phenotype due to beneficial adipose tissue remodelling at 12 weeks of HFD¹⁶. As expected, differentially expressed genes at 12 weeks enriched terms relating to tissue remodelling and inflammatory processes. Additionally, the *Positive Regulation of Metabolic Process* term was enriched indicating that IRF5-dependent metabolic adaptation may be sustained over time (Fig. 1L). Gene set enrichment analysis (GSEA) on GO terms

relating to the *TCA Cycle, Glycolytic Process* and *Regulation of the Type 1 Interferon Response* confirmed that genes related to cellular metabolism were disproportionately impacted by IRF5 deficiency (Fig. 1M). These findings indicate that IRF5-KO alters ATM metabolic adaptation to caloric excess and this is represented at the transcriptional level.

IRF5-deficiency is associated with increased oxidative respiration and fatty acid oxidation in the SVF of epididymal WAT upon caloric excess

To functionally characterise cellular respiration, we carried out metabolic flux analyses on the SVF of EpiWAT from IRF5-KO and WT mice following 4 weeks of HFD. Under conditions favouring mitochondrial respiration, EpiWAT SVF, largely composed of ATMs, had increased oxidative respiration in IRF5-KO relative to WT (Fig. 2A). This was also reflected by an increased area under the curve (AUC) (Fig. 2B). Interestingly, when evaluating oxygen consumption under conditions favouring glycolysis, we also found oxidative respiration to be increased in IRF5-KO under both basal and glucose-stimulated conditions (Fig. 2C). The energetic plot of basal and maximal respiration confirms the hyperoxidative nature of SVF from IRF5-KO relative to WT (Fig. 2D). To discern whether the increased oxidative respiration in IRF5-KO could be attributed to fatty acid oxidation (FAO), we carried out a palmitate (Palm) oxidation test with or without etomoxir (ETO), an inhibitor of carnitine palmitoyl transferase 1 (CPT1), the enzyme allowing palmitoyl-CoA catabolism²⁸. When treated with Palm, oxygen consumption was higher in cells from IRF5-KO mice relative to WT mice, but the difference between the genotypes was normalised when cells were treated with ETO (Fig. 2E, S2A). This indicates that CPT1-dependent FAO contributes to the higher mitochondrial oxidative respiration in SVF from IRF5-KO mice relative to WT mice. Following these findings in the SVF, we investigated the metabolic effects of IRF5-deficiency in bone marrow-derived macrophages (BMDMs) from IRF5-KO and WT mice. BMDMs were treated with bacterial lipopolysaccharides (LPS), a known stimulant of IRF5 expression, and with Palm to replicate lipotoxicity. We applied metabolic flux analyses and found no genotype-dependent difference in extracellular acidification rate in response to LPS or Palm, nor under basal conditions when testing glycolysis (Fig. S2B). In the same assay, oxygen consumption after glucose injection was increased in IRF5-KO relative to WT BMDMs following treatment with LPS or Palm. This indicates that mitochondrial respiration, aerobic glycolysis, or both, preferentially take place in IRF5-deficient macrophages (Fig. 2F, S2C). Carrying out a test of mitochondrial respiration, we observed no difference in untreated cells (Fig. S2D). Yet mitochondrial respiration was increased in IRF5-KO relative to WT BMDMs following treatment with LPS or Palm (Fig. 2G). The metabolic phenotype of BMDMs mirrors that seen in the SVF following 4 weeks of HFD (Fig. 2A), indicating that ATMs may be the main drivers of the difference in respiration seen in EpiWAT SVF from IRF5-KO and WT mice. The energetic plot from these experiments indicated that whilst extracellular acidification rate was similar between genotypes, oxygen consumption was consistently higher in IRF5-KO relative to WT BMDMs (Fig. 2H). The switch in metabolic adaptation in IRF5-KO coincided with lower concentrations of IL6 and TNF, and higher concentrations of IL10 secreted into cell culture media (Fig. 2I), confirming that IRF5-KO BMDMs are more prone to alternative polarisation, as previously described^{16,20,29}. Complementary to these experiments, we applied an inhibitory IRF5 decoy peptide (IRF5-

DP) to mature IRF5-competent BMDMs. IRF5-DP binds to IRF5 in the cytoplasm, preventing its nuclear translocation³⁰. LPS-induced upregulation of TNF is prevented by IRF5-DP, confirming that IRF5-DP blocks the transcriptional activity of IRF5 (Fig. 2J). When treated with Palm, oxygen consumption was increased with IRF5-DP relative to vehicle, which was reflected by increased oxygen consumption rate (OCR) at maximal respiration and increased AUC (Fig. 2K, S2E). The energetic plot reflects increased oxidative respiration in response to Palm and inducible by IRF5-DP (Fig. 2L). The effects of IRF5-DP delivery indicate a mechanism dependent on nuclear translocation and transcriptional activity and rule out a differentiation effect of IRF5-deficiency that may result in altered cellular respiration. We next used adenoviral delivery to re-introduce IRF5 expression in BMDMs from IRF5-KO mice. Treatment with an IRF5 adenovirus (adIRF5) resulted in a 1.4-fold increase in IRF5 expression (Fig. S2F) compared to the control adenovirus (adGFP). When metabolic flux was analysed following Palm treatment, OCR was decreased in cells treated with adIRF5, but not in cells treated with adGFP (Fig. 2M, S2G). To further link IRF5 to altered mitochondrial function, we ectopically overexpressed IRF5 in primary brown adipocytes as cells rich in mitochondria without an overt immune function. Adenoviral delivery of IRF5 in brown adipocytes resulted in a 5-fold increase in IRF5 expression relative to samples treated with adGFP (Fig. S2H). AdIRF5 treated cells were irresponsive to oligomycin and FCCP, had increased proton leak, and decreased ATP production and spare capacity (Fig. 2N, S2I). In adIRF5 treated cells, mitochondrial machinery is less able to respond to increased energy demand and respiration was no longer coupled to ATP production.

Altered destination of glycolysis end-products and accumulation of alpha-hydroxyglutarate characterise the TCA cycle in IRF5-deficient macrophages

Evaluating elements of mitochondrial respiration, we carried out targeted quantitative metabolomics of the tricarboxylic acid (TCA) cycle intermediates in IRF5-KO and WT BMDMs treated for 2 h or 24 h with Palm or with LPS. Global correlative analyses of metabolite concentrations resulted in a strong positive correlation ($p < 0.0001$; $R^2 = 0.42$) between genotypes and indicated overall higher concentrations of TCA metabolites in IRF5-KO BMDMs (Fig. 3A). PCA score plot obtained from metabolite concentrations revealed genotype-dependent separation of the TCA cycle metabolite profile with Palm treatment for 2 h and following LPS treatment for 24 h (Fig. 3B, S3A). Variable ranking per principal component revealed that alpha-hydroxyglutarate (AHG) was the highest contributor to the IRF5-dependent response to 2 h Palm (Fig. 3C). Accordingly, AHG concentration was increased in IRF5-KO BMDMs (Fig. 3D). Surprisingly little is known about AHG in macrophage metabolism. Previous reports link this metabolite to inhibition of alpha-ketoglutarate (AKG) dehydrogenase³¹, which is supported by our findings of reciprocal regulation of AKG and accumulation of its precursor glutamine in IRF5-KO. As reflected by PCA plots following 2 h of treatment, IRF5-dependent remodelling of the TCA metabolite landscape is a specific and early response to Palm. In response to LPS, most metabolites in IRF5-KO cells are normalised to WT levels (Fig. S3B). Taking TCA metabolite profile into consideration with correlative analyses per metabolite (Fig. 3E), IRF5-deficiency seems to modify the destination of glycolysis end-products (lactate/pyruvate) as well as AHG or glutamine to AKG conversion (Fig. 3F). Despite considerable remodelling of TCA cycle intermediates in IRF5-KO cells, this alone cannot explain increased

mitochondrial respiration nor the inflammatory profile of IRF5-KO cells. Thus, we characterised structural aspects of mitochondria that may alter function. We first evaluated mitochondrial density through electron microscopy and found no genotype-dependent differences (Fig. 3G, S3C). We also observed no difference in form factor nor aspect ratio, proxies of mitochondrial dynamics³² (Fig. S3D). However, analysing membrane associations with mitochondria revealed that IRF5-KO BMDMs are characterised by lower proportions of distant (> 30 nm) mitochondria-endoplasmic reticulum contacts (MERC), relative to WT BMDMs upon treatment with Palm (Fig. 3H, S3E). Taken together, these data indicate that IRF5 plays a role in maintaining normal TCA cycle responses to Palm or LPS. Frequency of distant MERCs is also decreased in IRF5-KO relative to WT in response to Palm. However, these findings cannot explain the increased mitochondrial respiration in IRF5-KO BMDMs in response to metabolic stress.

IRF5 binds and regulates mitochondrial matrix protein GHITM in macrophages

To investigate potential mechanisms, we first made use of previously published IRF5 ChIP-seq data³³. This dataset originates from a chromatin immunoprecipitation of IRF5 in BMDMs treated with LPS for 30 and 120 minutes. At 30 and 120 minutes of LPS stimulation, we mapped 3404 and 526 genes with IRF5 binding, respectively. Functional classification revealed that 2.3% and 5.1% of bound genes, at 30 and 120 minutes of LPS treatment, are part of the *Immune System Process* GO term; whereas 17.8% and 14.6% were in the *Metabolic Process* GO term (Fig. 4A). These results indicate that IRF5 directly binds to genes that control metabolic as well as immune processes in macrophages.

Whilst the above indicated that IRF5 binds to genes that can impact cellular metabolism upon LPS treatment, our current data indicated a time-dependent and divergent metabolic response to LPS and to Palm under the control of IRF5. To investigate these responses at the transcriptional level, we carried out RNA-seq on IRF5-KO and WT BMDMs following 2 h or 24 h treatment with LPS or with Palm. To ensure *in vivo* relevance of these analyses, we also included our RNA-seq analyses on F4/80⁺ ATMs sorted from EpiWAT of IRF5-KO and WT mice on HFD for 4 weeks and 12 weeks (Fig. 1L). To genes filtered on differential expression, we applied clustering analyses to define 6 clusters based on expression trajectory over time (Fig. 4B). Of the 6 clusters defined, 4 were differentially regulated between IRF5-KO and WT BMDMs upon LPS or Palm treatment; whereas upon HFD, 3 clusters were differentially regulated between genotypes (Fig. 4B). GO term enrichment of differentially regulated clusters indicated several clusters related to the regulation of transcription, cellular metabolic processes as well as myeloid cell differentiation and tissue remodelling (Fig. S4A). Differentially regulated clusters upon Palm treatment related to response to lipids, induction of immune tolerance as well as mitochondrial respiration, these were also enriched in ATMs upon HFD. Interestingly, correlative analyses of gene expression also found that Palm treatment resulted in the most divergent IRF5-dependent response (Fig. S4B). To define target genes differentially regulated upon inflammatory, lipotoxic and *in vivo* metabolic stress, we carried out differential expression analyses between genotypes on the different models. Importantly, Palm treatment resulted in the highest number of differentially expressed genes between IRF5-KO and WT cells, followed by LPS and HFD (Fig. 4C). One percent of differentially expressed genes were represented in all conditions (Fig. 4D), and integrating these data with the previously reported IRF5 ChIP-seq allowed us to

identify a subset of 6 genes that are differentially regulated between IRF5-KO and WT cells and are also bound by IRF5 at, or upstream of, their transcription start sites (*ATF5*, *SYCE2*, *ABCG1*, *LRRC27*, *FNIP2*, *GHITM*) (Fig. 4E). Of these genes, *GHITM* has been reported to have an overt function in maintaining the mitochondrial network as well as inner membrane cristae³⁴. Interestingly, correlative analyses in IRF5-competent cells revealed that *GHITM* was negatively correlated with IRF5 expression in ATMs (Fig. 4F). These data indicate that IRF5 controls the expression of *GHITM* in macrophages and this may be important in mediating repression of mitochondrial respiration. In line with the above results, we quantified the number and length of cristae per mitochondrion in ultra-structural analysis of IRF5-KO and WT BMDMs following Palm treatment and found indeed that both number and length of cristae per mitochondrion were increased in IRF5-KO BMDMs relative to WT (Fig. 4G). These data support that IRF5 may transcriptionally repress *GHITM* expression, and function, upon metabolic stress.

GHITM is highly expressed in monocytes and ATMs and its silencing reverses highly oxidative respiration in IRF5-deficiency

We procured previously published single cell RNA-seq data from EpiWAT SVF of mice on HFD for 6 and 12 weeks¹. Single cell sequencing data confirmed that IRF5 and *GHITM* are highly expressed in monocytes as well as in macrophages from EpiWAT SVF, expression levels were higher than all other targets identified (Fig. 5A, 5B, S5A). Correlative analyses revealed that *GHITM* expression was negatively correlated to IRF5 expression at the single cell level ($R = -0.44$; $p < 0.001$) (Fig. 5C). IRF5 expression was highest in monocytes, with its expression increasing over time. The negative correlation with *GHITM* was also sustained over time (Fig. 5B, 5D). Our analyses of this dataset, with our own data, suggests that that an interaction between IRF5 and *GHITM* may impact cellular respiration and metabolic adaptation of macrophages in diet-induced obesity. Thus, with guide RNAs (gRNA) targeting *GHITM* (g*GHITM*), we transduced BMDMs from mice with myeloid-restricted expression of the clustered regularly interspaced short palindromic repeats (CRISPR)-associated protein 9 (Cas9) linked to EGFP. We first confirmed Cas9-EGFP expression in mature BMDMs (Fig. S5B). Transfection with g*GHITM* resulted in a 40 % decrease in *GHITM* expression relative to controls (Fig S5C). We subjected this model to Palm treatment, where we confirmed decreased *GHITM* expression in response to Palm and upon transfection, by both qPCR and Western blotting (Fig. 5E, S5D). We also confirmed increased TNF expression in g*GHITM* transfected cells and upon Palm treatment (Fig. 5F). Metabolic flux analyses revealed that g*GHITM* transfection resulted in decreased oxidative respiration relative to controls, both under basal conditions and following Palm treatment, this effect was most pronounced at maximal respiration (Fig. 5G). To determine whether *GHITM* contributes to increased oxidative respiration in IRF5-deficient macrophages following lipotoxicity (Fig. 2G), we carried a double transfection with a gRNA targeting IRF5 (gIRF5) and with g*GHITM*. We first confirmed efficient knockdown of targeted genes, where gIRF5 resulted in a 40 % knockdown of IRF5 when used alone or simultaneously with g*GHITM*, which itself lowered *GHITM* expression to 30% (Fig. 5H). This model was treated with Palm and subjected to metabolic flux analysis. Transfection with gIRF5 alone increased OCR relative to controls, confirming our findings from IRF5-KO and WT mice and from treatment with IRF5-DP (Fig. 5I, 2G, 2K, S2E). This increase is normalised to control levels in cells doubly

transfected with gGHITM and gIRF5 (Fig. 5I). Taken together, these results indicate that GHITM contributes to increased oxidative respiration in IRF5-deficient macrophages.

IRF5 expression is associated with decreased GHITM expression and altered human monocyte and ATM metabolic phenotype

When we observed that IRF5 and GHITM were highly expressed in monocytes as well as macrophages, we sought to validate our results in monocytes from patients with T2D. We sorted CD14⁺ monocytes based on their expression of IRF5, and the sorted cells were subjected to RNA-seq (Fig. 6A). Paired differential expression analysis of IRF5⁺ versus IRF5⁻ negative monocytes revealed 3211 genes upregulated in IRF5⁺ monocytes versus 295 genes downregulated. GO term-enrichment of each gene set found that upregulated genes enriched terms relating to cell adhesion, development and motility (Fig. 6B). Interestingly, terms enriched amongst downregulated genes were related to mitochondrial organisation and protein localisation to mitochondria (Fig. 6B). Moreover, GHITM was consistently downregulated in IRF5⁺ relative to IRF5⁻ monocytes (Fig. 6C). Next, we stained cytospin prepared monocytes, from patients with T2D, with IRF5 and with an antibody against the oxidative phosphorylation (OXPHOS) enzyme complexes, known to be anchored to the mitochondrial cristae structures maintained by GHITM (Fig. 6D). We found that monocytes with primarily nuclear localisation of IRF5 (Nuc) had lower OXPHOS enzyme staining density relative to monocytes with cytoplasmic IRF5 staining (Cyt). Investigating adipose tissue, we quantified IRF5 and GHITM mRNA expression in CD14⁺ cells sorted from human WAT biopsies from obese patients. We separated patients based on IRF5 mRNA expression level and found that IRF5^{Hi} expressers have a lower expression of GHITM than IRF5^{Lo} expressers (Fig. 6E). Following these additional lines of evidence that IRF5 and GHITM share the same counter-regulation in human monocytes and ATMs as in mice, we sought to verify that IRF5 can indeed bind to GHITM in human macrophages as it does in murine macrophages (Fig. 4G). We used the University of California Santa Cruz (UCSC) genome browser to visualise IRF5 binding regions on or around the GHITM gene (Fig. 6F). Indeed, IRF5 can bind to several regions on and upstream of the GHITM gene. Furthermore, mRNA expression of GHITM is decreased in LPS-treated human monocyte-derived macrophages (HMDM) relative to untreated HMDMs; and this coincides with a decrease in active transcription histone mark H3K27ac in LPS-treated HMDMs relative to untreated HMDMs. The above analyses show that IRF5 and GHITM are expressed in human monocytes and macrophages, are reciprocally regulated, and that IRF5 can also bind to the GHITM gene. We next sought to functionally validate our hypothesis that IRF5 expression is associated with functional differences in cellular respiration in human monocytes and ATMs. We carried out flow cytometric analyses on human venous blood and AT SVF to quantify IRF5 expression in CD14⁺ monocytes and macrophages, and to analyse their metabolic adaptation. Correlative analyses indicated that ATM expression of IRF5 tends to negatively correlate with cellular lipid content, mitochondrial mass, activity, and activity-to-mass ratio, trends for lipid content and mitochondrial activity-to-mass ratio are also found in monocytes (Fig. 6G). We next quantified lipid content in IRF5⁺ and IRF5⁻ ATMs and found, similar to *in vivo* results, that IRF5⁺ ATMs were characterised by a lower lipid content relative to IRF5⁻ ATMs (Fig. 6H). We plotted monocyte and ATM populations onto an IRF5 and BODIPY quadrant, analyses confirmed that

IRF5⁺ cells are characterised by a restricted lipid pool and the IRF5⁺BODIPY⁺ population has the lowest frequency in both monocytes and ATMs (Fig. 6I). Taken together these findings indicate that IRF5 can bind to and transcriptionally regulate GHITM expression under metabolic stress in human monocytes and macrophages. This regulation has functional consequences on mitochondrial activity and on cellular lipid content which may be a key substrate for mitochondrial metabolism.

Discussion

Visceral WAT is a key responder to caloric excess. Adaptive responses dictate disease course in metabolic syndrome and a major determinant of tissue adaptation is the phenotype and function of ATMs. ATMs are a heterogeneous population of cells ranging from regulatory to highly inflammatory, the latter being a key contributor to systemic metabolic decline in obesity and T2D. As sentinel cells playing a homeostatic role in normal physiology, the molecular mechanisms of ATM adaptation to early caloric excess remain to be fully understood. Here we demonstrate that ATMs undergo extensive IRF5-dependent metabolic rewiring upon short-term caloric excess. ATM oxidative capacity is limited by IRF5-mediated transcriptional repression of GHITM, the inner mitochondrial membrane protein that maintains mitochondrial structure for efficient oxidative respiration. Decreased expression of GHITM and loss of cristae organisation bias macrophage metabolism away from mitochondrial respiration to promote inflammatory polarisation.

Previous studies show that inflammation arises in WAT and is mediated by ATMs. The key implication of IRF5 in metabolic inflammation and T2D has been demonstrated in both mice and humans¹⁶. Gain-of-function IRF5 risk-variants have also been associated with increasing macrophage glycolytic flux²⁵, a cellular process that supports inflammatory effector functions. A recent study has also demonstrated that IRF5 regulates airway macrophage metabolic response to viral infection³⁵. Whilst we have previously reported the inflammatory responsiveness of IRF5 in ATMs in metabolic disease, the role that this transcription factor plays in adapting ATM metabolism remains to be investigated. First, we investigated the potential role of IRF5 in regulating cellular metabolic adaptation through a model of short term high-fat feeding. A study by Lee *et al.*³⁶ demonstrated that immunocompromised mice developed insulin resistance upon short-term high-fat feeding, indicating that inflammation is not required for insulin resistance at this stage. A further study by Shimobayashi *et al.*³⁷ confirmed this finding, demonstrating that WAT was disproportionately affected and that early insulin resistance precedes inflammation. In our findings, we confirm that upon 4 weeks of high-fat feeding mice develop altered glucose homeostasis, whilst accumulating macrophages that are metabolically different to ATMs from mice on a NCD.

Reports in immunometabolism have characterised macrophage metabolic responses to infectious pathogens³⁸. Recent studies demonstrate that tissue macrophages have their own metabolic specificities in-line with microenvironmental pressures^{39,40}. Moreover, in T2D, a systemic abundance of metabolic substrates in the form of hyperglycaemia and dyslipidaemia presents its own challenges. In the case of ATMs, they reside in a lipid-rich environment and take on an overall hypermetabolic phenotype upon diet-

induced obesity, increasing glycolysis as well as mitochondrial respiration¹⁰. More recent studies report specific LAM expansion within 6 weeks of HFD, with LAMs being metabolically protective¹. Similarly, CD11c⁺, CD206⁺ double positive macrophages expressing the scavenger receptor MARCO are highly oxidative and expand in short-term HFD⁴¹. Whilst these two populations of ATMs are highly oxidative and represent physiological adaptation to caloric excess, the predominance of glycolysis has been associated with supporting ATM inflammatory effector function¹¹. In the current study, we demonstrate that IRF5-deficient macrophages have a higher rate of mitochondrial respiration relative to IRF5-competent macrophages. This indicates that IRF5 plays an important role in tilting the metabolic balance in ATMs towards glycolysis by impairing mitochondrial respiration, thus promoting metabolism that supports inflammation. Analysing the ways in which mitochondria are affected in IRF5-deficiency, we found that TCA metabolites are modified in IRF5-KO relative to WT macrophages upon stimulation. We initially expected typical perturbations to the TCA cycle in M1-like macrophages to be reversed in IRF5-KO. Notably, for itaconate and succinate to be depleted, as their accumulation is a hallmark of M1-like metabolism⁴². Yet, upon LPS stimulation, we were surprised to find that only succinate was decreased in IRF5-KO. Typically, succinate accumulation in M1-like macrophages is a result of the inhibition of succinate dehydrogenase by itaconate⁴³, yet we do not observe such co-regulation in our study. Indicating that IRF5-dependent mechanisms may be circumventing the characterised itaconate-succinate axis in macrophage polarisation. Some hallmarks of the IRF5-KO BMDM TCA cycle reproduce previous reports on TCA dynamics in the M2-like state. IRF5-KO BMDMs accumulate lactate in preference to pyruvate conversion at the end of glycolysis, this has been previously reported as characteristic of M2 macrophages in the tumour microenvironment⁴⁴⁻⁴⁷. In IRF5-KO BMDMs decreased pyruvate means it is less available as a substrate for mitochondrial metabolism. This is coherent with our *ex vivo* and human observations that IRF5-KO or IRF5^{L0} macrophages have a higher lipid content, which fuels mitochondrial FAO. The highest-ranking metabolite driving the IRF5-dependent response to Palm was AHG. AHG is a relatively little-known metabolite, it is produced as a result of non-canonical enzyme function at low pH (possibly due to increased lactate in IRF5-KO BMDMs)⁴⁸. AHG has been reported to accumulate in IL4-primed macrophages and is also found as an oncometabolite produced from mutated tumour-derived isocitrate dehydrogenase^{31,49,50}. AHG is a competitive inhibitor of AKG-dependent deoxygenases, occupying the same active sites on AKG^{31,48,49}. This action of AHG results in genome-wide histone and DNA methylation alterations. This mechanism is supported by our data as we do observe a concomitant decrease in AKG as well as an accumulation of glutamine in IRF5-KO. With the TCA metabolite landscape being altered, but not fully explaining the metabolic phenotype of IRF5-deficient macrophages, we carried out structural analyses of mitochondria in search of a structural basis for increased mitochondrial metabolism. With no difference in mitochondrial density nor dynamics, we investigated membrane interaction with the endoplasmic reticulum. MERCs play diverse roles, including in metabolic sensing, and lipid and calcium ion transport⁵¹⁻⁵³. MERCs have been extensively studied in other cell types, and only to a limited extent in macrophages⁵⁴. Studies in fibroblasts show that narrower MERCs are associated with more efficient calcium ion and lipid exchange with mitochondria; whilst increasing MERC distance is associated with dormancy and loss of lipid homeostasis^{51,55}. The proportion of distant MERCs (> 30 nm)

was decreased in IRF5-KO relative to WT macrophages upon stimulation with Palm. However, the stability of narrower associations indicates that increased respiration is independent of MERC-mediated substrate transfer in our model.

In a data-driven approach, we combined public datasets with our own RNA-seq data to reveal a previously undescribed IRF5-dependent mechanism that impairs macrophage mitochondrial respiration. Impaired mitochondrial respiration is, at least in part, attributed to decreased expression of GHITM. GHITM was initially characterised as an inner mitochondrial membrane protein required to maintain cristae structures, the anchoring points for OXPHOS enzyme complexes³⁴. Previous studies found that GHITM downregulation causes mitochondrial fragmentation and cristae disorganisation³⁴. Mitochondrial fragmentation has previously been associated with inflammatory polarisation, both in response to LPS and to fatty acids^{56,57}. Studies in lymphocyte cell lines stimulated with inflammatory cytokines and from virus-exposed monocytes also report downregulation of GHITM^{58,59}. These previous reports are in line with our current findings that loss of GHITM is associated with inflammation. We additionally report a role for GHITM in macrophages and in ATMs in both humans and mice in response to metabolic stress. In summary, we have deciphered a novel mechanism through which IRF5, a well characterised pro-inflammatory transcription factor, alters cellular mitochondrial dynamics and respiration. Having identified this IRF5-dependent mechanism to control cellular metabolism, a number of questions remain unanswered. For example, to elucidate how and through which regulatory elements IRF5 may be binding to such non-inflammatory targets as GHITM. Whilst it is widely accepted that IRF5, and other IRFs, target interferon sensitive regulatory elements (ISRE), the presence and significance of ISREs on metabolically relevant genes remains to be investigated. Furthermore, the specific functional contribution of GHITM downregulation to effective inflammation is unknown, for example consequent mitochondrial fragmentation may be a source of reactive oxygen species required for bacterial killing. Similarly, whilst we observe increased oxidative respiration in IRF5-deficiency, we also observe an increase in the intracellular lipid pool, the significance and composition of this lipid pool remains to be understood, future investigations can decipher whether the interferon pathway can also act on cellular lipid dynamics. Lastly, despite several lines of evidence implicating IRF5 in metabolic decline associated with diet-induced obesity, the metabolic stressors that induce IRF5 expression remain unknown. Future work on the above questions will be of important mechanistic insight into how this influential pathway can be modulated in diabetes and in other inflammatory conditions.

Methods

Human samples

Blood samples and adipose tissue biopsies were obtained from different populations admitted to the Lariboisière and Geoffroy Saint Hilaire hospitals (Paris, France). Studies were conducted in accordance with the Helsinki Declaration and were registered to a public trial registry (Clinicaltrials.gov; NCT02671864). The Ethics Committee of CPP Ile-de-France approved the clinical investigations for all individuals, and written informed consent was obtained from all individuals. The principal investigator of

this clinical trial is Prof. Jean-François Gautier: jean-francois.gautier@aphp.fr. Adipose tissue biopsies were obtained from obese subjects during bariatric surgery.

Experimental animals and *In vivo* studies

Male C57BL/6J mice (5-7 weeks) were purchased from Charles River. To generate mice with a myeloid-specific deletion of IRF5, IRF5 flox/flox mice (C57BL/6-Irf5^{tm1Ppr}/J; stock no. 017311) were crossed with LysM-Cre mice (B6.129P2-Lyz2^{tm1}(cre)Ifo/J; stock no. 04781), purchased from The Jackson Laboratory. To generate mice with a restricted myeloid expression of the Cas9 endonuclease, Rosa26-Cas9KI mice (Gt(ROSA)26Sortm1.1(CAG-cas9*,-EGFP)Fezh/J; stock no. 024858, The Jackson Laboratory) were crossed with LysM-Cre mice.

Mice carrying mutated alleles were identified by PCR screening performed on genomic DNA (DNeasy Blood & Tissue Kit, Qiagen) with specific primers (Table S1). Mice were housed at 22°C on a 12 h light/dark cycle in the “Centre d’Explorations Fonctionnelles” of Sorbonne University (UMS-28). All mice used in the study were male and aged between 7-10 weeks old at the time of the experiment starting point. All animal experiments were approved by the French ethical board (Paris-Sorbonne University, Charles Darwin N°5, 01026.02) and conducted in accordance with the guidelines stated in the International Guiding Principles for Biomedical Research Involving Animals.

Mice were fed with High Fat Diet (HFD) (60% fat, D12492, Research Diets) or normal chow diet for 4 weeks. Mice had *ad libitum* access to food and water. Mice were weighed weekly and glycaemia measured.

For oral glucose tolerance test (GTT), mice were fasted overnight before being gavaged with glucose (2g/kg of body weight). Tail vein blood was collected to measure glycaemia with a glucometer (Verio, One touch). For insulin tolerance test (ITT), mice were fasted during 5 h before being i.p injected with insulin (0,5U/kg of body weight). For pyruvate tolerance test (PTT), mice were fasted overnight before being i.p. injected with pyruvate (2g/kg of body weight). Glycaemia was monitored for 120 min after insulin or pyruvate injection.

Organ collection and histology

Mice were sacrificed by cervical dislocation. Upon dissection, tissues were weighed. Immediately after collection, samples were either digested with collagenase, snap-frozen for further analysis or drop-fixed into 10% formalin (Sigma Aldrich) for 24 h for histological analysis. For histological analysis, tissues were processed for dehydration, clearing and paraffin embedding with an automated carousel (Leica). Sections (6µM thick) were stained with hematoxylin and eosin according to standard procedures. Images were acquired with a slide scanner (Zeiss Axio Scan Z1).

Stromal vascular fraction

The stromal vascular fraction (SVF) containing mononuclear cells and preadipocytes was isolated from the adipose tissue after collagenase digestion. Briefly, adipose tissue biopsies were minced in collagenase solution (1mg/ml collagenase (C6885, Sigma Aldrich), diluted in Dulbecco's Modified Eagle Medium (DMEM) (Gibco) supplemented with 1% penicillin/streptomycin (P/S), Hepes and 2% BSA) for 20 min at 37°C. Lysate was then passed through a 200µM filter. After centrifugation, the resulting cell pellet was resuspended in red blood cell lysis buffer (155mM NH₄Cl, 12mM NaHCO₃, 0,1mM EDTA) and passed through a 70µM filter. Cells were centrifuged and resuspended in FACS buffer (1X PBS supplemented with 0,5% BSA and 5mM EDTA) for further analysis.

Brown adipocytes and adenoviral transduction

Brown adipose tissue (BAT) depots were dissected from euthanized 10-14 weeks old C57BL/6J mice. SVF was isolated as described. Cells were plated in cell culture medium (DMEM supplemented with 10% fetal bovine serum (FBS) and 1% P/S for two days. Brown adipocytes differentiation was induced with cell culture medium containing 10% FBS, 1% P/S, 20 nM insulin, 1 nM triiodothyronine, 0,125 mM indomethacin, 5 µM dexamethasone and 0,5 mM 3-isobutyl-1-methylxanthine (IBMX) for two days. Afterwards, cells were placed back in cell culture medium containing 10% FBS, 1% P/S, 20 nM insulin and 1 nM triiodothyronine for 4 days. Brown adipocytes were incubated with adenovirus particles for 48 h, at MOI 10.

Flow cytometry and cell sorting

SVF cells were prepared as described above. Blood cells were obtained from 1 ml of venous blood after red blood cells lysis and resuspended in FACS buffer.

Cells were incubated with an Fc-blocker (120-000-422, Miltenyi Biotec) for 10 min. For metabolic analysis, cells were incubated with either 200 µM JC-1 (T3168, ThermoFisher Scientific) or 14.6 µM 2-NBDG (N13195, ThermoFisher Scientific) for 30 min at 37°C. Finally, cells were stained for surface markers (Table S2) and a Live/Dead viability dye (L34957, ThermoFisher Scientific) according to manufacturer's protocol. For IRF5 staining, cells were fixed with Foxp3-staining kit (00-5523-00, ThermoFisher Scientific) and then stained with an anti-IRF5 (10547-1-AP, Proteintech) for 1 h, and then with a secondary PE antibody (12-4739-81, ThermoFisher Scientific) for 30 min.

Acquisition was performed on a MACSQuant cytometer (Miltenyi Biotec). Cell sorting was performed on a FACSAria III (BD Biosciences). Cells were directly sorted in RLT lysis buffer supplemented with β-mercaptoethanol for RNA extraction (Qiagen). Data were analysed with FlowJo software (Tree Star).

Cells from the previously isolated SVF were stained for immunoselection of F4/80⁺ cells according to manufacturer's protocol (MACS, Miltenyi Biotec). Cells were resuspended in MACS buffer (1X PBS supplemented with 0.5% BSA and 2mM EDTA) containing the appropriate dilution of anti-F4/80 microbeads (130-110-443, Miltenyi Biotec), for 10 min at 4°C. Automated magnetic cell separation was performed with the Multi-MACS Cell Separator. Once collected, the F4/80⁺ cell fraction was washed and

directly resuspended in RLT lysis buffer supplemented with β -mercaptoethanol for RNA extraction (Qiagen).

***In vitro* macrophage studies**

Bone marrow-derived macrophages: Murine bone marrow cells were isolated from femurs and tibias. Cells were plated in DMEM (Gibco) supplemented with 10% FBS, 1% P/S and 30% L929 conditioned-media and were allowed to differentiate for 8-10 days into bone marrow-derived macrophages.

Treatments: Cells were treated with LPS (10ng/ml) (L2630, Sigma Aldrich) or Palmitate (200 μ M) for the appropriate time. Palmitate stock solution was prepared by dissolving sodium palmitate (P9767, Sigma Aldrich) in 50% ethanol solution, followed by dilution in a 1% fatty acid free albumin solution (A8806, Sigma Aldrich).

Decoy peptide: Fully differentiated BMDMs were pre-treated with an IRF5 decoy peptide³⁰ (50 μ g/ml) for 30 min, before being treated for further analysis.

Transfection: Fully differentiated BMDMs were transfected with IRF5 (Mm.Cas9.IRF5.1.AB, Integrated DNA Technologies) or GHITM (Mm.Cas9.GHITM.1.AA, Integrated DNA Technologies) gRNA (30nM) complexed with lipofectamine RNAiMAX (ThermoFisher Scientific) for 48 h.

Cytokine quantification: Pro-inflammatory cytokines in the cell culture supernatants were quantified with the Mouse Inflammation Kit (552364, BD Cytometric Bead Array) according to manufacturer's protocol.

Immunofluorescence

After red blood cells lysis, blood cells were cytospun onto SuperFrost Plus slides. Samples were fixed in 10% formalin (Sigma Aldrich) then stained for CD14 (13-0149-82, Invitrogen) overnight and with the appropriate secondary antibody (Streptavidin AF 647, S32357, ThermoFisher Scientific). Samples were then permeabilized and stained for IRF5 (10547-1-AP, Proteintech) and OXPHOS (MS604, Abcam) with the appropriate secondary antibodies (goat anti-mouse FITC (A11001) and anti-rabbit AF555 (A21428), Invitrogen). Nuclei were counterstained with Hoescht 33342 (ThermoFisher Scientific). Images were acquired with a confocal microscope (Zeiss LSM 710) and analysed with ImageJ® (Fiji).

Quantitative PCR with reverse transcription

RNA was extracted from cells or tissue using RNeasy Plus Mini or Micro kit (Qiagen). Complementary DNA was synthesized with M-MLV Reverse Transcriptase kit (Promega). SYBR Green qRT-PCR reactions were performed with MESA green MasterMix (Eurogentec) and sequence-specific primers (Table S3), using QuantStudio 3 Real-Time PCR Systems (ThermoFisher Scientific). 18S was used for normalization to quantify relative mRNA expression levels.

Western blotting

To extract proteins, cells were lysed in RIPA lysis buffer (Sigma), supplemented with proteases (A32955, ThermoFisher Scientific) and phosphatases inhibitors (1862495, ThermoFisher Scientific). Proteins were separated on NuPAGE 4-12% polyacrylamide gels (ThermoFisher Scientific) and then transferred onto nitrocellulose membranes. Membranes were probed with the appropriate primary (anti-GHITM, 16296-1-AP, Proteintech; anti-Actin, ab8226, Abcam) and secondary antibodies (31430 and 31460, Invitrogen) and visualized with SuperSignal West Pico Substrate (34080, ThermoFisher Scientific). Images were analysed with ImageJ® (Fiji).

Metabolic flux measurements

Real-time extracellular acidification rate (ECAR) and oxygen consumption rate (OCR) were measured using Seahorse XF24 or XFe96 extracellular flux analyser (Agilent). Briefly, cells were differentiated in XF24 or XFe96 cell culture plate (15,000 to 30,000 cells per well). Adipose stromal vascular cells (800,000 cells per well) were seeded in an XFe96 cell culture plate pretreated with CellTak (Corning). Cells were incubated in Seahorse XF base medium supplemented with either 2 mM L-glutamine, 10mM glucose and 1mM sodium pyruvate (pH=7.4) for mitochondrial stress test or only 2 mM L-glutamine (pH=7.4) for glycolysis stress test, for 1 h at 37°C in a non-CO₂ incubator. For palmitate oxidation test, cells were placed in substrate limited medium (DMEM supplemented with 0,5 mM glucose, 1 mM GlutaMAX (Life Technologies), 0,5mM carnitine and 1% FBS) for 24 h. Assay was performed in fatty acid oxidation assay buffer (111mM NaCl, 4.7mM KCl, 1.25 mM CaCl₂, 2 mM MgSO₄, 1.2 mM NaH₂PO₄, 2.5 mM glucose, 0.5mM carnitine, 5mM HEPES, pH=7.4). Cells were pre-treated with Etomoxir (40µM) and then with palmitate (175µM) before the assay. ECAR and OCR were measured in response to injections of either glucose (10mM), oligomycin (1µM) and 2-deoxyglucose (2-DG) (50mM) for glycolysis stress test or oligomycin (1µM), carbonyl cyanide 4-(trifluoromethoxy) phenylhydrazone (FCCP) (1µM) and rotenone/antimycin A (0.5µM) for mitochondrial stress and palmitate oxidation tests. All compounds were purchased from Sigma-Aldrich. Three measurements were made under basal conditions and after each drug injection. Each measurement cycle had the following time parameters: 'mix' 3 min, 'wait' 2 min, 'measure' 3 min.

Electron microscopy and structural analyses

BMDMs were scraped and fixed in 2 % glutaraldehyde for 2 h at 4°C, postfixed in 1 % Osmium tetroxide for 1 h at 4°C, dehydrated, and embedded in Epon. Samples were then cut using an RMC/MTX ultramicrotome (Elexience), and ultrathin sections (60-80 nm) were mounted on copper grids, contrasted with 8% uranyl acetate and lead citrate, and observed with a Jeol 1200 EX transmission electron microscope (Jeol LTD) equipped with a MegaView II high-resolution transmission electron microscopy camera. Pictures of cells sections were taken at 45000 × magnification. For MERC analyses, mitochondria and ER limits were traced on ImageJ® (Fiji). The fraction of mitochondrial membrane in contact with ER within a 50-nm range was calculated and normalized to the mitochondrial perimeter and expressed as the total percent of contact according to different ranges of distance between both organelles⁶⁰. Mitochondria number per section was also measured to evaluate mitochondria density.

For cristae analysis, mitochondria and cristae were outlined using ImageJ® (Fiji) and both the total length and number of cristae in each mitochondrion was calculated, as previously described⁶¹. For the analysis of mitochondria dynamics, the long and short axis of each mitochondria, as well as their perimeter and area, were measured. From these values, aspect ratio (major axis/minor axis) and form factor (perimeter)²/(4×pixArea) were calculated. TEM analyses were performed in triplicate and a minimum of 11 images per sample were taken.

Quantification of TCA metabolites by liquid chromatography coupled to high resolution mass spectrometry (LC-HRMS)

Metabolite extraction. A volume of 170 µL of ultrapure water was added to the frozen cell pellets. At this step, 20µL of each sample were withdrawn for further determining the total protein concentration (colorimetric quantification / Pierce BCA Protein Assay Kit, ThermoFisher Scientific). Then, 10 µL of 11 internal standards at 50 µg/mL were added to the remaining 150 µL of cell lysate: 13C5-alpha-hydroxyglutaric acid, 13C2-phosphoenolpyruvic acid, 13C4-fumaric acid, 13C3-pyruvic acid, 13C4-succinic acid (Merck), and D4-citric acid, 13C5-glutamine, D3-malic acid, 13C4,15N-aspartic-acid, 13C5-alpha-ketoglutaric-acid and 13C5-glutamic acid (Eurisotop), followed by a volume of 350 µL of cold methanol. Resulting samples were left on ice for 90 min. After a final centrifugation step at 20,000 g for 15 min at 4°C, supernatants were recovered and dried under a stream of nitrogen using a TurboVap instrument (ThermoFisher Scientific) and stored at -80°C until analysis. Prior to LC-HRMS analysis, dried extracts were dissolved in 100 µL of 40 µL of chromatographic mobile phase A + 60 µL of mobile phase B (see below).

Preparation of calibration standards. Working solution (WS) for calibration curves and quality control solutions were prepared from two separate mother solutions (100 µg/ml in water) of each quantified compound : L-glutamic acid, L-aspartic acid , L-glutamine, succinic acid, alpha-ketoglutaric acid, trans-aconitic acid, L-(-)-malic acid, D,L-isocitric acid, D-glyceric acid, fumaric acid, citric acid, pyruvic acid, D-alpha-hydroxyglutaric acid disodium salt, D-(-)-lactic acid, D-(-)-3-phosphoglyceric acid, phosphoenolpyruvic acid and itaconic acid (all from Sigma). Several diluted solutions of calibration standard solutions (CSS) and quality control solutions (QCS) were prepared by successive two-fold dilutions of WS in ultrapure water. Then, a three-fold dilution in a BSA solution (7200 µg/mL), of each previous diluted solution (CSS1-8 and QCS1-3) was applied to prepare standards for the calibration curve (from 33.33 to 0.26 µg/mL) and quality control (from 53.33 to 1.51 µg/mL). A volume of 350µL of cold methanol was added to each calibration curve and quality control solutions and followed metabolite extraction process.

LC-HRMS analysis. Targeted LC-HRMS experiments were performed using an U3000 liquid chromatography system coupled to a Q Exactive Plus mass spectrometer (ThermoFisher Scientific). The software interface was Xcalibur (version 2.1) (ThermoFisher Scientific). The mass spectrometer was externally calibrated before each analysis in ESI- polarity using the manufacturer's predefined methods and recommended calibration mixture. The LC separation was performed on a Sequant ZIC-pHILIC 5 µm,

2.1 x 150 mm column (HILIC) maintained at 45°C (Merck, Darmstadt, Germany). Mobile phase A consisted of an aqueous buffer of 10 mM of ammonium acetate, and mobile phase B of 100% acetonitrile. Chromatographic elution was achieved with a flow rate of 200 µL/min. After injection of 10 µL of sample, elution started with an isocratic step of 2 min at 70% B, followed by a linear gradient from 70 to 40% of phase B from 2 to 7 min. The chromatographic system was then rinsed for 5 min at 0% phase B, and the run was ended with an equilibration step of 9 min. The column effluent was directly introduced into the electrospray source of the mass spectrometer, and analyses were performed in the negative ion mode. The Q Exactive Plus mass spectrometer was operated with capillary voltage set at -2.5 kV and a capillary temperature set at 350°C. The sheath gas pressure and the auxiliary gas pressure (nitrogen) were set at 60 and 10 arbitrary units, respectively. The detection was achieved from m/z 50 to 600 in the negative ion mode and at a resolution of 70,000 at m/z 200 (full width at half maximum). All metabolites were detected as their deprotonated [M-H]⁻ species.

Succinic acid, glyceric acid, itaconic acid, and lactic acid were detected at m/z 117.01933 (retention time (rt): 4.50 min); 105.01933 (rt 3.20 min); 129.01933 (rt 3.73 min); 89.02441 (rt 2.40 min), respectively; and quantified using ¹³C₄-succinic acid (m/z 121.03251) as internal standard (ISTD). Malic acid and aconitic acid were monitored at m/z 133.01424 (rt 6.70 min); 173.0091 (rt 7.15 min), respectively; and quantified with D₃-malic acid (m/z 136.03276). Citric acid, isocitric acid and 3-phospho glyceric acid were monitored at m/z 191.01944 (rt 7.80); 191.01952 (rt 8.35); 184.98566 (rt 7.70 min) respectively; and quantified with D₄-citric acid (m/z 195.04455). Pyruvic acid (m/z 87.00876, rt 2.25 min), aspartic acid (m/z 132.03023, rt 5.20 min), glutamine (m/z 145.06186, rt 4.75 min), glutamic acid (m/z 146.04588 rt 4.80 min), alpha-hydroxyglutaric acid (m/z 147.02989, rt 6.20 min), alpha-ketoglutaric acid (m/z 152.04637, rt 6.50 min), fumaric acid (m/z 150.03072, rt 7.05 min), and phosphoenolpyruvic acid (m/z 166.97509, rt 8.20 min) were all quantified with their isotopically labeled homologues (see above).

Metabolomic data processing and quantification. Xcalibur software was used for peak detection and integration. Metabolite quantification was performed using calibration curves established from peak area ratios between metabolites and their respective internal standard. Each metabolite amount was normalised by the protein quantity measured in each sample by BCA assay.

RNA-sequencing of BMDMs and F4/80⁺ ATMs

After extraction, total RNA was analysed using Agilent RNA 6000 Pico Kit on the Agilent 2100 Bioanalyzer System. RNA quality was estimated based on capillary electrophoresis profiles using the RNA Integrity Number (RIN) and DV200 values. RNA sequencing libraries were prepared using the SMARTer Stranded Total RNA-Seq Kit v2 - Pico Input Mammalian (Clontech/Takara) from 10ng of total RNA. This protocol includes a first step of RNA fragmentation using a proprietary fragmentation mix at 94°C. The time of incubation was set up for all samples at 4 min, based on the RNA quality, and according to the manufacturer's recommendations. After fragmentation, indexed cDNA synthesis and amplification were performed followed with a ribodepletion step using probes targeting mammalian rRNAs. PCR amplification was finally achieved on ribodepleted cDNAs, using 12 cycles estimated in accordance to the

input quantity of total RNA. Library quantification and quality assessment were performed using Qubit fluorometric assay (Invitrogen) with dsDNA HS (High Sensitivity) Assay Kit and LabChip GX Touch using a High Sensitivity DNA chip (Perkin Elmer). Libraries were then equimolarly pooled and quantified by qPCR using the KAPA library quantification kit (Roche). Sequencing was carried out using a pair-end 2 x 100 bp mode on the NovaSeq 6000 system (Illumina), targeting between 10 and 15M clusters per sample.

STAR v2.7.3a (Spliced Transcripts Alignment To a Reference) was used to align reads to the mouse mm10 genome and generate raw counts⁶². We processed normalization and differential expression gene analysis with DESeq2⁶³. Pathway enrichment analyses were performed using clusterProfiler⁶⁴ with differentially expressed genes ($\text{abs}(\log_2\text{FoldChange}) > 1.3$ and/or $\text{adj p-value} < 0.05$). Gene set enrichment analyses were performed using GSEA v4.0.1⁶⁵ with genes pre-ranked by $\text{sign}(\log_2\text{FoldChange}) * [-\log_{10}(\text{pvalue})]$.

RNA-sequencing of IRF5^{+/-} human monocytes

Complementary DNA libraries and RNA sequencing Library preparation and Illumina sequencing were performed at the *Ecole Normale Supérieure* genomic core facility (Paris, France). 20 ng of total RNA were amplified and converted to cDNA using SMART-Seq v4 Ultra Low Input RNA kit (Clontech). Afterwards an average of 150 pg of amplified cDNA was used to prepare library following Nextera XT DNA kit (Illumina). Libraries were multiplexed by 12 on a high-output flowcells. A 75 bp read sequencing was performed on a NextSeq 500 device (Illumina). A mean of $38,9 \pm 8$ million passing Illumina quality filter reads was obtained for each of the 12 samples.

The analyses were performed using the Eoulsan pipeline⁶⁶, including read filtering, mapping, alignment filtering, read quantification, normalisation and differential analysis: Before mapping, poly N read tails were trimmed, reads ≤ 40 bases were removed, and reads with quality mean ≤ 30 were discarded. Reads were then aligned against the hg19 genome from Ensembl version 91 using STAR (version 2.5.2b)⁶². Alignments from reads matching more than once on the reference genome were removed using Java version of samtools⁶⁷. To compute gene expression, hg19 GTF genome annotation version 91 from Ensembl database was used. All overlapping regions between alignments and referenced exons were counted and aggregated by genes using HTSeq-count 0.5.3⁶⁸. The sample counts were normalized using DESeq2 1.8.1⁶⁹. Statistical treatments and differential analyses were also performed using DESeq2 1.8.1.

Statistics

Data analysis were performed using Microsoft Excel for Mac 16.47. Statistical analysis was performed using a two-tailed t-test for two groups, an ordinary one-way ANOVA followed by Tukey's multiple-comparisons test for multiple groups and a two-way ANOVA followed by Bonferroni's multiple comparison test on Prism 9 for macOS (GraphPad). Correlative analyses were performed on Prism 9 for macOS, computing Pearson coefficients for normally distributed data or Spearman coefficients for non-

normally distributed data (GraphPad). PCA analyses were carried out on Prism 9 for macOS. Trajectory-resolved clustering was carried out on the Orange (v. 3.28.0) Python toolbox⁷⁰. Statistical approaches per data panel are detailed in figure legends.

Public data

Single cell sequencing data: Single cell sequencing data from Jaitin *et al.*¹, were downloaded and treated using BioTuring BBrowser (v. 2.7.48)⁷¹. Data were filtered in BBrowser and exported in tabular format for subsequent treatment with Microsoft Excel for Mac and Prism9 for macOS.

UCSC genome browser: Gene tracks in Fig. 6E were visualised with the UCSC genome browser <http://genome.ucsc.edu>^{72,73}, using the track hubs⁷⁴. JASPAR2020 was used to visualise transcription factor binding sites⁷⁵. The BLUEPRINT track-set was used for RNA expression and H3K27Ac lines^{76,77}. Sample lines and tracks available through this [session link](#) / [live link](#). The Human Dec. 2013 (GRCh38/hg38) assembly was used^{78,79}.

Data availability

Data that support findings of this study are available from the corresponding authors upon request. RNA-sequencing of IRF5^{+/-} human monocytes: RNASeq gene expression data and raw fastq files are available on the GEO repository (www.ncbi.nlm.nih.gov/geo/) under accession number: GSEXXX. Source data are provided with this paper.

Declarations

Competing interests

The authors declare no competing interests

Author contributions: LO, NV and FA conceived and designed the study. LO, TE, RB, JM, JC, CP, AH, FC and FA performed experiments and collected data. LO, TE, AH, MD, CP, CB, SL, JR and FA analysed data. AH, MD, JM, PL, LGB, SB, SL, CB, FF and FAC contributed data or analysis tools. JBJ, DL, JB, AS, JPR, JR and JFG provided key resources. LO, DL, JB, JPR, JR, JFG, NV and FA provided intellectual input. LO, NV and FA wrote the manuscript.

Acknowledgements: Image acquisitions or cytometric analysis and sorting were done at CHIC (*Centre d'Histologie, d'Imagerie Cellulaire et de Cytométrie*, Centre de Recherche des Cordeliers UMR S 1138, Paris, France). CHIC is a member of the SU Cell Imaging and Flow Cytometry network (LUMIC) and UPD cell imaging networks. Transmission electronic microscopy was performed at CIQLE platform (Centre d'Imagerie Quantitative Lyon-Est, Lyon, France) and we thank Elisabeth Errazuriz and Christel Cassin for their technical help. High-throughput sequencing has been performed by the ICGex NGS platform of the Institut Curie supported by the grants ANR-10-EQPX-03 (Equipex) and ANR-10-INBS-09-08 (*France*

Génomique Consortium) from the French National Research Agency (*Agence Nationale de la Recherche; ANR*; "Investissements d'Avenir" program), by the Canceropole Ile-de-France and by the SiRIC- Curie program - SiRIC Grant "INCa-DGOS-4654". This research was supported by the French National Research Agency (*Agence Nationale de la Recherche; ANR*) ANR-JCJC grant for the MitoFLAME Project ANR-19-CE14-0005 and by the French Society for Diabetes (*Société Francophone du Diabète; SFD*) Allocation Exceptionnelle to FA. Support was provided to FA and NV through a collaboration with AstraZeneca. Support was provided to FA and JFG by the European Foundation for the Study of Diabetes. Support was also provided to FC and FF by the *Commissariat à l'Energie Atomique et aux Energies Alternatives* and the MetaboHUB infrastructure (ANR-11-INBS-0010 grant). N.V. was supported by grants from the European Union H2020 framework (ERC-EpiFAT 725790) and the French National Research Agency (*Agence Nationale de la Recherche; ANR*) ANR-PUMAs.

References

1. Jaitin, D.A., *et al.* Lipid-Associated Macrophages Control Metabolic Homeostasis in a Trem2-Dependent Manner. *Cell* **178**, 686-698 e614 (2019).
2. Coats, B.R., *et al.* Metabolically Activated Adipose Tissue Macrophages Perform Detrimental and Beneficial Functions during Diet-Induced Obesity. *Cell Rep* **20**, 3149-3161 (2017).
3. Hill, D.A., *et al.* Distinct macrophage populations direct inflammatory versus physiological changes in adipose tissue. *Proc Natl Acad Sci U S A* **115**, E5096-E5105 (2018).
4. Pirzgalska, R.M., *et al.* Sympathetic neuron-associated macrophages contribute to obesity by importing and metabolizing norepinephrine. *Nat Med* **23**, 1309-1318 (2017).
5. Sarvari, A.K., *et al.* Plasticity of Epididymal Adipose Tissue in Response to Diet-Induced Obesity at Single-Nucleus Resolution. *Cell Metab* **33**, 437-453 e435 (2021).
6. Weisberg, S.P., *et al.* Obesity is associated with macrophage accumulation in adipose tissue. *J Clin Invest* **112**, 1796-1808 (2003).
7. O'Neill, L.A., Kishton, R.J. & Rathmell, J. A guide to immunometabolism for immunologists. *Nat Rev Immunol* **16**, 553-565 (2016).
8. Palsson-McDermott, E.M. & O'Neill, L.A.J. Targeting immunometabolism as an anti-inflammatory strategy. *Cell Res* **30**, 300-314 (2020).
9. Angelin, A., *et al.* Foxp3 Reprograms T Cell Metabolism to Function in Low-Glucose, High-Lactate Environments. *Cell Metab* **25**, 1282-1293 e1287 (2017).
10. Serbulea, V., *et al.* Macrophage phenotype and bioenergetics are controlled by oxidized phospholipids identified in lean and obese adipose tissue. *Proc Natl Acad Sci U S A* **115**, E6254-E6263 (2018).
11. Boutens, L., *et al.* Unique metabolic activation of adipose tissue macrophages in obesity promotes inflammatory responses. *Diabetologia* **61**, 942-953 (2018).
12. Zhu, X., *et al.* Micro-environment and intracellular metabolism modulation of adipose tissue macrophage polarization in relation to chronic inflammatory diseases. *Diabetes Metab Res Rev* **34**,

- e2993 (2018).
13. Prieur, X., *et al.* Differential lipid partitioning between adipocytes and tissue macrophages modulates macrophage lipotoxicity and M2/M1 polarization in obese mice. *Diabetes* **60**, 797-809 (2011).
 14. Sharma, M., *et al.* Enhanced glycolysis and HIF-1alpha activation in adipose tissue macrophages sustains local and systemic interleukin-1beta production in obesity. *Sci Rep* **10**, 5555 (2020).
 15. Xu, X., *et al.* Obesity activates a program of lysosomal-dependent lipid metabolism in adipose tissue macrophages independently of classic activation. *Cell Metab* **18**, 816-830 (2013).
 16. Dalmas, E., *et al.* Irf5 deficiency in macrophages promotes beneficial adipose tissue expansion and insulin sensitivity during obesity. *Nat Med* **21**, 610-618 (2015).
 17. Hedl, M., Yan, J., Witt, H. & Abraham, C. IRF5 Is Required for Bacterial Clearance in Human M1-Polarized Macrophages, and IRF5 Immune-Mediated Disease Risk Variants Modulate This Outcome. *J Immunol* **202**, 920-930 (2019).
 18. Yanai, H., *et al.* Role of IFN regulatory factor 5 transcription factor in antiviral immunity and tumor suppression. *Proc Natl Acad Sci U S A* **104**, 3402-3407 (2007).
 19. Krausgruber, T., *et al.* IRF5 promotes inflammatory macrophage polarization and TH1-TH17 responses. *Nat Immunol* **12**, 231-238 (2011).
 20. Weiss, M., *et al.* IRF5 controls both acute and chronic inflammation. *Proc Natl Acad Sci U S A* **112**, 11001-11006 (2015).
 21. Alzaid, F., *et al.* IRF5 governs liver macrophage activation that promotes hepatic fibrosis in mice and humans. *JCI Insight* **1**, e88689 (2016).
 22. Byrne, A.J., *et al.* A critical role for IRF5 in regulating allergic airway inflammation. *Mucosal Immunol* **10**, 716-726 (2017).
 23. Corbin, A.L., *et al.* IRF5 guides monocytes toward an inflammatory CD11c(+) macrophage phenotype and promotes intestinal inflammation. *Sci Immunol* **5**(2020).
 24. Duffau, P., *et al.* Promotion of Inflammatory Arthritis by Interferon Regulatory Factor 5 in a Mouse Model. *Arthritis Rheumatol* **67**, 3146-3157 (2015).
 25. Hedl, M., Yan, J. & Abraham, C. IRF5 and IRF5 Disease-Risk Variants Increase Glycolysis and Human M1 Macrophage Polarization by Regulating Proximal Signaling and Akt2 Activation. *Cell Rep* **16**, 2442-2455 (2016).
 26. Reers, M., *et al.* Mitochondrial membrane potential monitored by JC-1 dye. *Methods Enzymol* **260**, 406-417 (1995).
 27. Bassaganya-Riera, J., Misyak, S., Guri, A.J. & Hontecillas, R. PPAR gamma is highly expressed in F4/80(hi) adipose tissue macrophages and dampens adipose-tissue inflammation. *Cell Immunol* **258**, 138-146 (2009).
 28. Cao, T., *et al.* Fatty Acid Oxidation Promotes Cardiomyocyte Proliferation Rate but Does Not Change Cardiomyocyte Number in Infant Mice. *Front Cell Dev Biol* **7**, 42 (2019).

29. Weiss, M., Blazek, K., Byrne, A.J., Perocheau, D.P. & Udalova, I.A. IRF5 is a specific marker of inflammatory macrophages in vivo. *Mediators Inflamm* **2013**, 245804 (2013).
30. Weihrauch, D., *et al.* An IRF5 Decoy Peptide Reduces Myocardial Inflammation and Fibrosis and Improves Endothelial Cell Function in Tight-Skin Mice. *PLoS One* **11**, e0151999 (2016).
31. Xu, W., *et al.* Oncometabolite 2-hydroxyglutarate is a competitive inhibitor of alpha-ketoglutarate-dependent dioxygenases. *Cancer Cell* **19**, 17-30 (2011).
32. Picard, M., White, K. & Turnbull, D.M. Mitochondrial morphology, topology, and membrane interactions in skeletal muscle: a quantitative three-dimensional electron microscopy study. *J Appl Physiol (1985)* **114**, 161-171 (2013).
33. Saliba, D.G., *et al.* IRF5:RelA interaction targets inflammatory genes in macrophages. *Cell Rep* **8**, 1308-1317 (2014).
34. Oka, T., *et al.* Identification of a novel protein MICS1 that is involved in maintenance of mitochondrial morphology and apoptotic release of cytochrome c. *Mol Biol Cell* **19**, 2597-2608 (2008).
35. Albers, G.J., *et al.* IRF5 regulates airway macrophage metabolic responses. *Clin Exp Immunol* (2021).
36. Lee, Y.S., *et al.* Inflammation is necessary for long-term but not short-term high-fat diet-induced insulin resistance. *Diabetes* **60**, 2474-2483 (2011).
37. Shimobayashi, M., *et al.* Insulin resistance causes inflammation in adipose tissue. *J Clin Invest* **128**, 1538-1550 (2018).
38. O'Neill, L.A. & Pearce, E.J. Immunometabolism governs dendritic cell and macrophage function. *J Exp Med* **213**, 15-23 (2016).
39. Daemen, S. & Schilling, J.D. The Interplay Between Tissue Niche and Macrophage Cellular Metabolism in Obesity. *Front Immunol* **10**, 3133 (2019).
40. Liu, Y., *et al.* Metabolic reprogramming in macrophage responses. *Biomark Res* **9**, 1 (2021).
41. Brunner, J.S., *et al.* The PI3K pathway preserves metabolic health through MARCO-dependent lipid uptake by adipose tissue macrophages. *Nat Metab* **2**, 1427-1442 (2020).
42. Mills, E.L., *et al.* Succinate Dehydrogenase Supports Metabolic Repurposing of Mitochondria to Drive Inflammatory Macrophages. *Cell* **167**, 457-470 e413 (2016).
43. Meiser, J., *et al.* Pro-inflammatory Macrophages Sustain Pyruvate Oxidation through Pyruvate Dehydrogenase for the Synthesis of Itaconate and to Enable Cytokine Expression. *J Biol Chem* **291**, 3932-3946 (2016).
44. Ivashkiv, L.B. The hypoxia-lactate axis tempers inflammation. *Nat Rev Immunol* **20**, 85-86 (2020).
45. Liao, Z.X., Fa, Y.C., Kempson, I.M. & Tseng, S.J. Repolarization of M2 to M1 Macrophages Triggered by Lactate Oxidase Released from Methylcellulose Hydrogel. *Bioconjug Chem* **30**, 2697-2702 (2019).
46. Zhang, W., *et al.* Lactate Is a Natural Suppressor of RLR Signaling by Targeting MAVS. *Cell* **178**, 176-189 e115 (2019).
47. Batie, M., *et al.* Hypoxia induces rapid changes to histone methylation and reprograms chromatin. *Science* **363**, 1222-1226 (2019).

48. Intlekofer, A.M., *et al.* L-2-Hydroxyglutarate production arises from noncanonical enzyme function at acidic pH. *Nat Chem Biol* **13**, 494-500 (2017).
49. Mu, L., *et al.* The IDH1 Mutation-Induced Oncometabolite, 2-Hydroxyglutarate, May Affect DNA Methylation and Expression of PD-L1 in Gliomas. *Front Mol Neurosci* **11**, 82 (2018).
50. Puchalska, P., *et al.* Isotope Tracing Untargeted Metabolomics Reveals Macrophage Polarization-State-Specific Metabolic Coordination across Intracellular Compartments. *iScience* **9**, 298-313 (2018).
51. Giacomello, M. & Pellegrini, L. The coming of age of the mitochondria-ER contact: a matter of thickness. *Cell Death Differ* **23**, 1417-1427 (2016).
52. Phillips, M.J. & Voeltz, G.K. Structure and function of ER membrane contact sites with other organelles. *Nat Rev Mol Cell Biol* **17**, 69-82 (2016).
53. Theurey, P. & Rieusset, J. Mitochondria-Associated Membranes Response to Nutrient Availability and Role in Metabolic Diseases. *Trends Endocrin Met* **28**, 32-45 (2017).
54. Martinvalet, D. The role of the mitochondria and the endoplasmic reticulum contact sites in the development of the immune responses. *Cell Death Dis* **9**, 336 (2018).
55. Area-Gomez, E., *et al.* Upregulated function of mitochondria-associated ER membranes in Alzheimer disease. *EMBO J* **31**, 4106-4123 (2012).
56. Zezina, E., *et al.* Mitochondrial fragmentation in human macrophages attenuates palmitate-induced inflammatory responses. *Biochim Biophys Acta Mol Cell Biol Lipids* **1863**, 433-446 (2018).
57. Kapetanovic, R., *et al.* Lipopolysaccharide promotes Drp1-dependent mitochondrial fission and associated inflammatory responses in macrophages. *Immunol Cell Biol* **98**, 528-539 (2020).
58. Nagel, J.E., *et al.* Identification of genes differentially expressed in T cells following stimulation with the chemokines CXCL12 and CXCL10. *BMC Immunol* **5**, 17 (2004).
59. Moni, M.A. & Lio, P. Network-based analysis of comorbidities risk during an infection: SARS and HIV case studies. *BMC Bioinformatics* **15**, 333 (2014).
60. Weaver, D., Bartok, A., Csordas, G. & Hajnoczky, G. A Standardized Method to Quantify ER-Mitochondrial Interfaces in Electron Micrographs. *Biophysical Journal* **112**, 133a-133a (2017).
61. Sood, A., *et al.* A Mitofusin-2-dependent inactivating cleavage of Opa1 links changes in mitochondria cristae and ER contacts in the postprandial liver. *P Natl Acad Sci USA* **111**, 16017-16022 (2014).
62. Dobin, A., *et al.* STAR: ultrafast universal RNA-seq aligner. *Bioinformatics* **29**, 15-21 (2013).
63. Love, M.I., Huber, W. & Anders, S. Moderated estimation of fold change and dispersion for RNA-seq data with DESeq2. *Genome Biology* **15**(2014).
64. Yu, G.C., Wang, L.G., Han, Y.Y. & He, Q.Y. clusterProfiler: an R Package for Comparing Biological Themes Among Gene Clusters. *Omics* **16**, 284-287 (2012).
65. Subramanian, A., *et al.* Gene set enrichment analysis: A knowledge-based approach for interpreting genome-wide expression profiles. *P Natl Acad Sci USA* **102**, 15545-15550 (2005).

66. Jourden, L., Bernard, M., Dillies, M.A. & Le Crom, S. Eoulsan: a cloud computing-based framework facilitating high throughput sequencing analyses. *Bioinformatics* **28**, 1542-1543 (2012).
67. Li, H., *et al.* The Sequence Alignment/Map format and SAMtools. *Bioinformatics* **25**, 2078-2079 (2009).
68. Anders, S., Pyl, P.T. & Huber, W. HTSeq—a Python framework to work with high-throughput sequencing data. *Bioinformatics* **31**, 166-169 (2015).
69. Love, M.I., Huber, W. & Anders, S. Moderated estimation of fold change and dispersion for RNA-seq data with DESeq2. *Genome Biol* **15**, 550 (2014).
70. Demsar, J., *et al.* Orange: Data Mining Toolbox in Python. *J Mach Learn Res* **14**, 2349-2353 (2013).
71. Le, T., *et al.* BBrowser: Making single-cell data easily accessible. *bioRxiv*, 2020.2012.2011.414136 (2020).
72. Kent, W.J., *et al.* The human genome browser at UCSC. *Genome Res* **12**, 996-1006 (2002).
73. Navarro Gonzalez, J., *et al.* The UCSC Genome Browser database: 2021 update. *Nucleic Acids Res* **49**, D1046-D1057 (2021).
74. Raney, B.J., *et al.* Track data hubs enable visualization of user-defined genome-wide annotations on the UCSC Genome Browser. *Bioinformatics* **30**, 1003-1005 (2014).
75. Fornes, O., *et al.* JASPAR 2020: update of the open-access database of transcription factor binding profiles. *Nucleic Acids Research* **48**, D87-D92 (2020).
76. Fernandez, J.M., *et al.* The BLUEPRINT Data Analysis Portal. *Cell Syst* **3**, 491+ (2016).
77. Adams, D., *et al.* BLUEPRINT to decode the epigenetic signature written in blood. *Nat Biotechnol* **30**, 224-226 (2012).
78. Lander, E.S., *et al.* Initial sequencing and analysis of the human genome. *Nature* **409**, 860-921 (2001).
79. Kent, W.J. & Haussler, D. Assembly of the working draft of the human genome with GigAssembler. *Genome Res* **11**, 1541-1548 (2001).

Figures

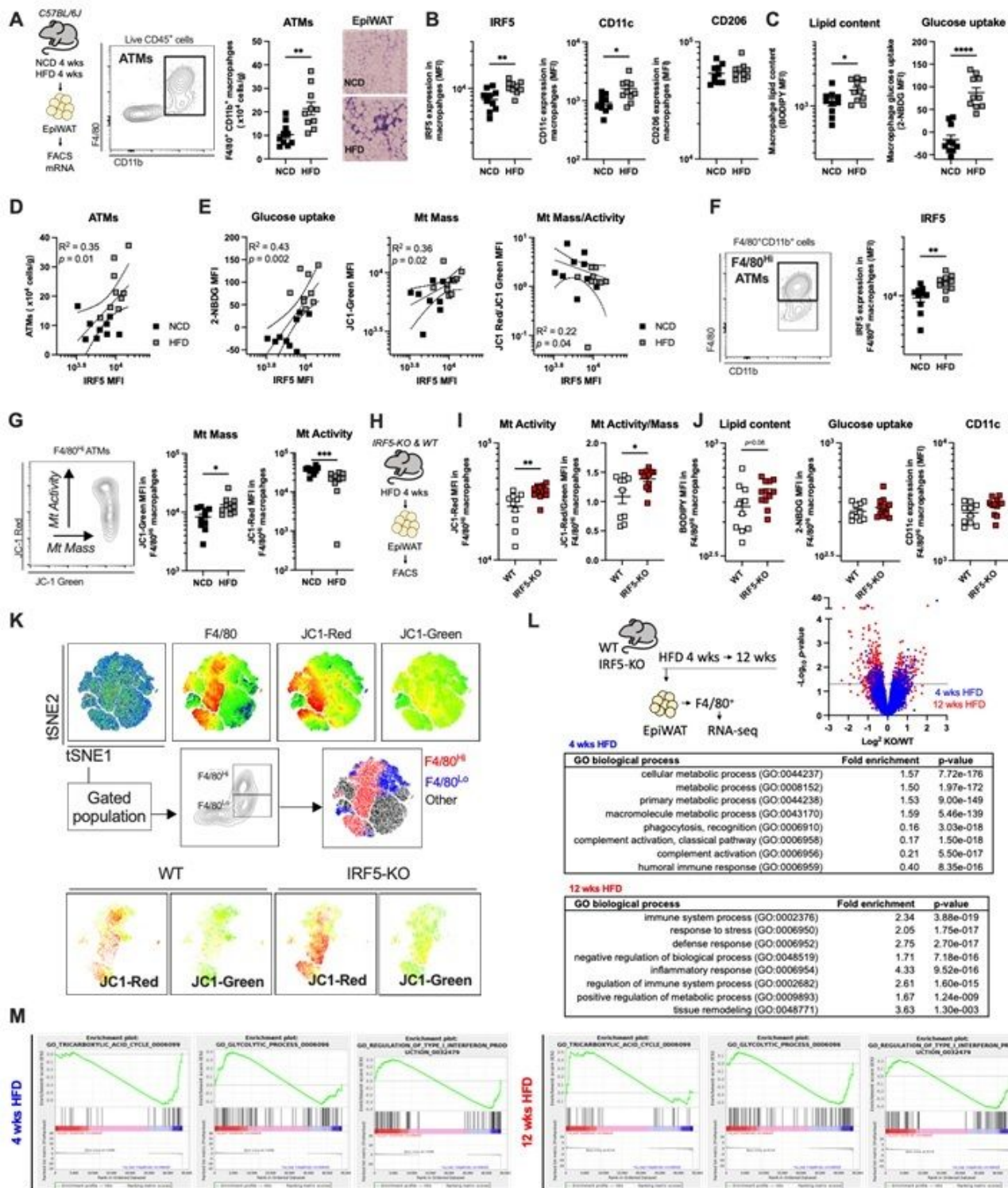


Figure 1

Epididymal white adipose tissue macrophages undergo IRF5-dependent metabolic adaptation upon short- and long-term high-fat feeding. A. C57BL/6J mice were placed on a high-fat diet (HFD) or normal chow diet (NCD) for 4 weeks (n=10 per group), epididymal white adipose tissue (EpiWAT) was disrupted and F4/80+CD11b+ adipose tissue macrophages (ATMs) were quantified by flow cytometry (**p=0.0023 unpaired t-test). Haematoxylin and eosin (HE) staining of epididymal fat pad at 5 x magnification to

visualise crown-like structures. B. Median fluorescence intensity (MFI) of IRF5, CD11c and CD206 in ATMs (**p=0.0041 and *p=0.0143 unpaired t-tests). C. MFI of BODIPY and 2-NBDG fluorescence in ATMs (*p=0.03 and ****p<0.0001 unpaired t-tests). D. Correlative analyses between IRF5 MFI and EpiWAT ATM numbers (R² = 0.35; p = 0.0104). E. Correlative analyses between IRF5 MFI, 2-NBDG MFI (R² = 0.43; p = 0.002), mitochondrial (Mt) mass (R² = 0.36; p = 0.02) and Mt Activity-to-Mass ratio (R² = 0.22; p = 0.04). F. MFI of IRF5 in EpiWAT F4/80Hi ATMs (**p=0.004 unpaired t-test). G. MFI of JC-1 Green and JC-1 red fluorescence, respectively markers of Mt mass and Mt activity, in EpiWAT F4/80Hi ATMs (*p=0.01 and ***p=0.0009 unpaired t-tests). H. Mice with a myeloid-deficiency of IRF5 (IRF5-KO) or their wild-type (WT) littermates were placed on HFD for 4 weeks (n=10 WT and n=12 IRF5-KO). EpiWAT was disrupted for ATM analysis by FACS. I. MFI of JC-1 Red fluorescence and ratio to JC-1 Green fluorescence, respective markers of Mt activity and ratio of activity-to-mass in ATMs from WT and IRF5-KO mice (**p=0.0032 and *p=0.019 unpaired t-test). J. MFI of BODIPY, 2-NBDG and CD11c fluorescence in ATMs from WT and IRF5-KO mice (p=0.08 unpaired t-tests). K. tSNE plot of MFI profiles of the stromal vascular fraction of EpiWAT of WT and IRF5-KO mice, overlay heatmap represents MFI of single markers and gated populations represent ATMs. L. WT and IRF5-KO mice were placed on HFD for 4 or 12 weeks and F4/80+ cells were sorted from EpiWAT for RNA sequencing. Differentially expressed genes (-log₁₀ p > 1.3) between genotypes at each time point were applied to gene ontology (GO) term enrichment analysis. M. Gene set enrichment analysis (GSEA) per time point. For correlations, Pearson correlation coefficients were calculated for parametric data and Spearman correlation coefficients were calculated for non-parametric data.

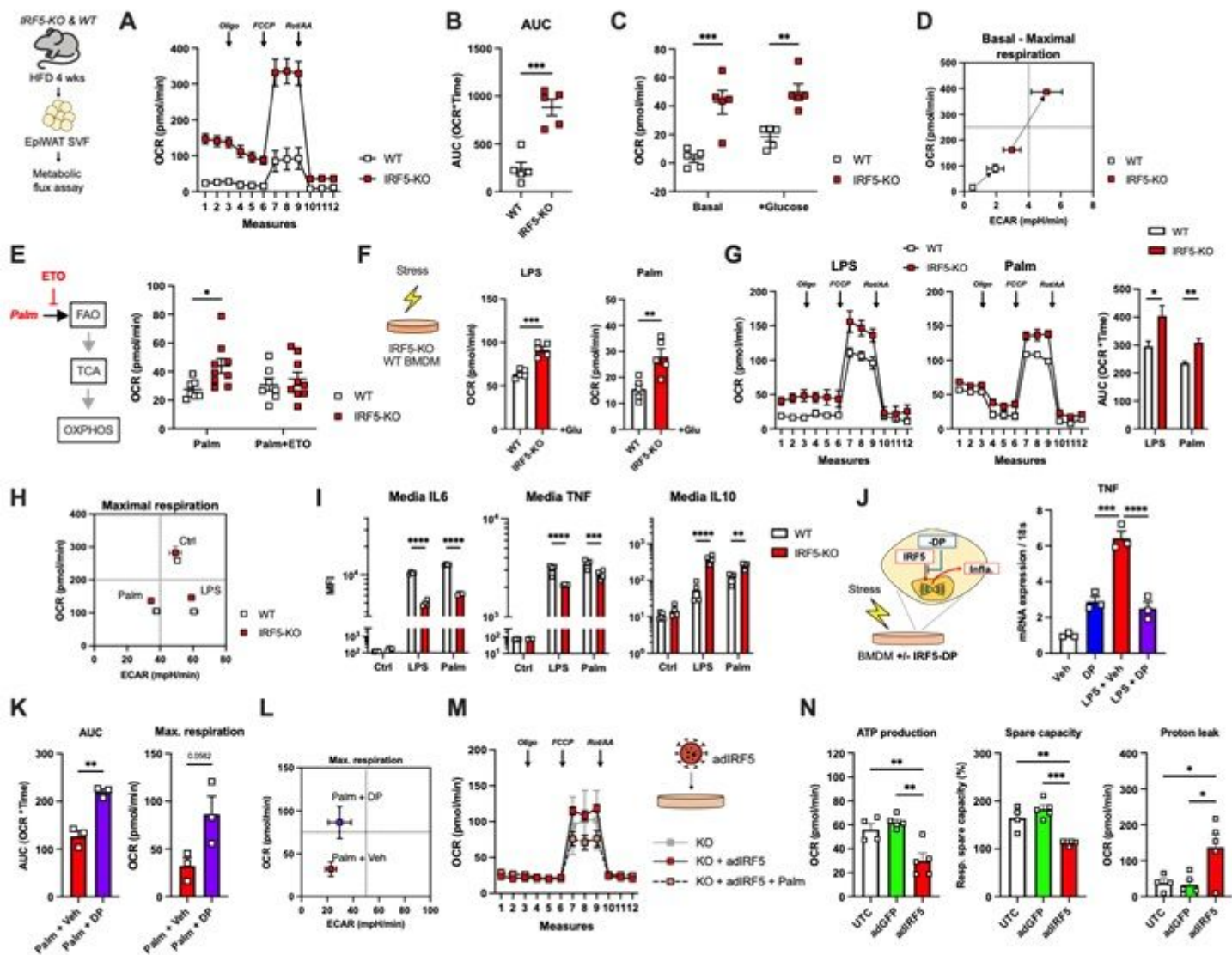


Figure 2

Myeloid-deficiency of IRF5 increases mitochondrial respiration in stromal vascular cells following high-fat diet and in bone marrow-derived macrophages. Mice with a myeloid-deficiency of IRF5 (IRF5-KO) or their wild-type (WT) littermates were placed on HFD for 4 weeks. Epididymal white adipose tissue (EpiWAT) was disrupted and the stromal vascular fraction (SVF) subjected to metabolic flux analysis. **A**. Mitochondrial stress test measuring oxygen consumption rate (OCR) of SVF from WT (n=5) and IRF5-KO (n=5) EpiWAT SVF upon administration of oligomycin (Oligo), carbonyl cyanide 4-(trifluoromethoxy) phenylhydrazone (FCCP) and rotenone/antimycin A (Rot/AA). **B**. Area under the curve (AUC) of mitochondrial stress test in **A**. (***) $p=0.0003$ unpaired t-test). **C**. OCR from glycolysis stress test under basal conditions and following addition of glucose (***) $p=0.0002$ and (**) $p=0.0018$ two-way ANOVA). **D**. Energetic plot of basal and maximal OCR and ECAR. **E**. Maximal OCR from Fig. S2A of fatty acid oxidation (FAO) test on SVF from WT (n=7) and IRF5-KO (n=9) mice (* $p=0.035$ one-way ANOVA). Palm, palmitate; ETO, etomoxir; TCA, tricarboxylic acid cycle; OXPHOS, oxidative phosphorylation. **F**. Bone

marrow-derived macrophages (BMDM) from WT (n=5) and IRF5-KO (n=5) mice were treated with lipopolysaccharides (LPS) or palmitate (Palm). OCR following addition of glucose (Glu) from glycolysis stress test in Fig. S2B. (LPS ***p=0.0001 and Palm **p=0.008 unpaired t-test). G. Mitochondrial stress test as in A. in BMDMs from WT and IRF5-KO mice following treatment with LPS or Palm. AUC of mitochondrial stress test (n=3 per genotype; *p=0.03 and **p=0.0027 unpaired t-test). H. Energetic plot of maximal respiration. ECAR from Fig. S2B and OCR from G and Fig. S2D. I. Cytokine quantification in media from WT and IRF5-KO BMDMs following treatment with LPS or Palm. Median fluorescence intensity (MFI) of IL6, TNF or IL10 coated beads (n=4 per genotype and per condition; IL6: ****p<0.0001 for both; TNF ****p<0.0001 and ***p=0.0002; IL10: ****p<0.0001 and **p=0.002 two-way ANOVA). J. BMDMs from C57BL/6J were treated with an IRF5-decoy peptide (DP) or a vehicle (Veh) and with LPS. RNA expression of TNF was quantified (***p=0.0002 and ****p<0.0001 one-way ANOVA). K. AUC and maximal respiration from mitochondrial stress test on BMDMs (n=3 per condition) treated with Palm and with IRF5-DP or with Veh. (**p=0.0022 and p=0.0582 unpaired t-test). L. Energetic plot of maximal respiration from mitochondrial stress test Fig. S2E. M. Metabolic flux analysis of BMDMs from IRF5-KO mice treated with Palm and with an IRF5 adenovirus (adIRF5) (n=3 per group). N. Primary brown adipocytes were treated with an IRF5 adenovirus (adIRF5) or a GFP control adenovirus (adGFP). ATP production (*p=0.0196, **p=0.0047), spare capacity (**p=0.0019, ***p=0.0002) and proton leak (*p=0.033, *p=0.017) calculated from mitochondrial stress test in Fig. S2J.

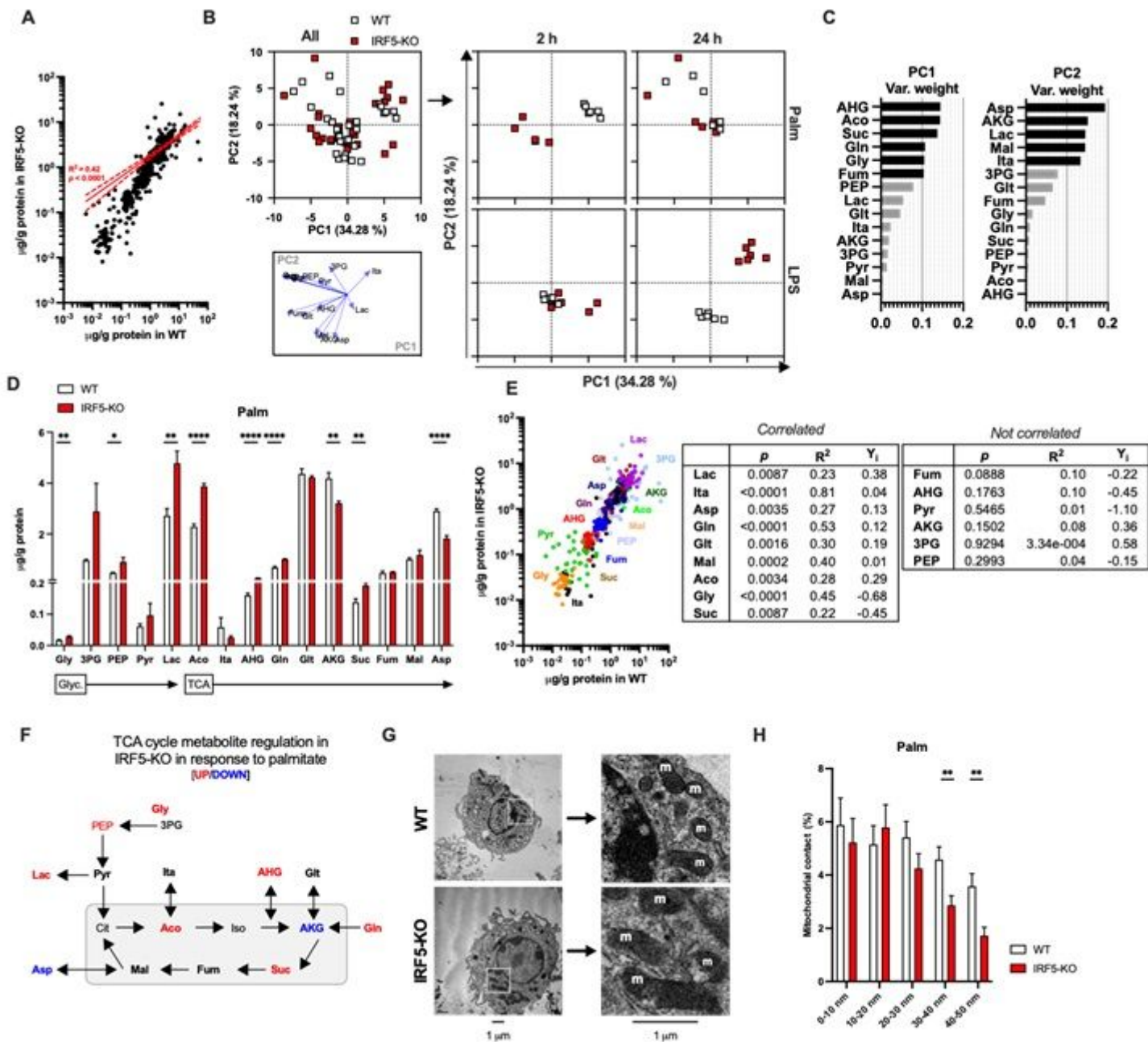


Figure 3

IRF5-deficiency alters glycolysis end-products and TCA cycle intermediates in bone marrow-derived macrophages. Bone marrow-derived macrophages (BMDM) from IRF5-KO or WT mice were treated with either LPS or palmitate (Palm) for 2 or 24 h. Targeted metabolomics analyses were carried out to quantify intracellular tricarboxylic acid (TCA) cycle metabolites and electron microscopy was carried out to evaluate mitochondrial structural characteristics (n=3 per condition). A. Correlative analyses of intracellular TCA cycle metabolites in BMDMs from IRF5-KO and WT mice ($R^2 = 0.42$, $p < 0.0001$). B. Principal component analysis (PCA) on TCA cycle metabolites. Samples separated based on time and treatment. C. Variable weighting from PCA, percent variance contribution to principal components (PC)1 and 2. D. Absolute quantification of TCA cycle metabolites in BMDMs from WT and IRF5-KO mice

following treatment with Palm for 2 h. (left to right: **p=0.002, *p=0.03, **p=0.004, ****p<0.0001, ***p<0.0001, ***p<0.0001, **p=0.002, **p=0.002, ***p<0.0001). E. Correlative analyses per metabolite. F. Schematic representation of metabolites with increased (red) or decreased (blue) abundance in IRF5-KO relative to WT BMDMs following treatment with Palm. G. Electron micrograph and magnified inlet of BMDMs from WT and IRF5-KO mice. Mitochondria are marked by 'm'. H. Percentage of mitochondrial membrane in contact with endoplasmic reticulum (ER) at different mitochondria-ER contact (MERC) site distances in BMDMs from WT and IRF5-KO mice following 2-hour treatment with Palm (**p=0.007, **p=0.003, n=3, unpaired t-test).

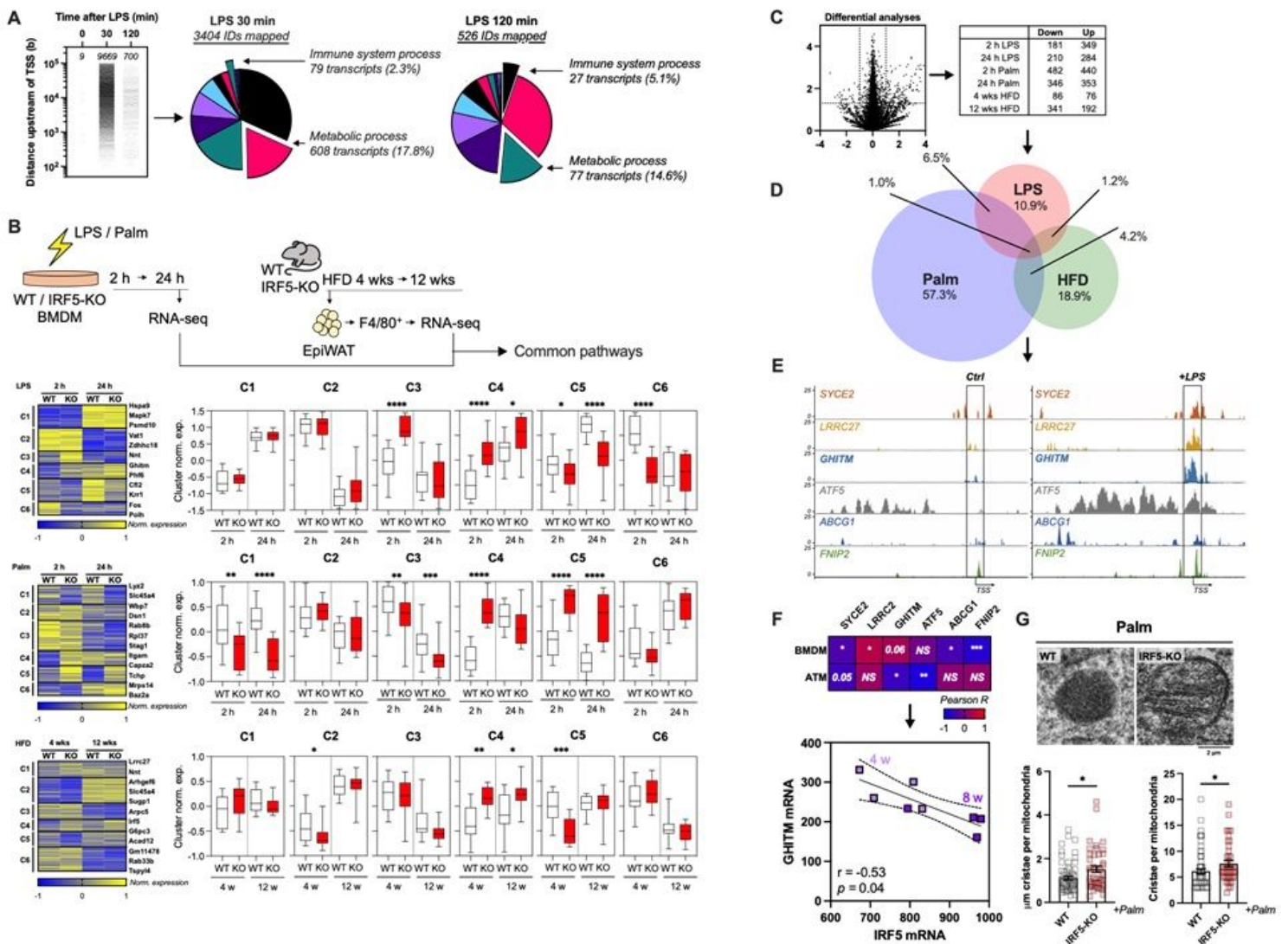


Figure 4

IRF5 binds to genes controlling cellular metabolism in bone marrow-derived and in adipose tissue macrophages. A. Publicly available chromatin immunoprecipitation (ChIP) seq of IRF5 in bone marrow-derived macrophages (BMDM) treated with lipopolysaccharides (LPS) for 30 or 120 min was procured. Peaks of interest were determined as either at or upstream of transcription start sites (TSS). Annotated genes were subjected to gene ontology (GO) enrichment analyses. B. Clustering analysis on RNA sequencing from BMDMs from mice with a myeloid-deficiency of IRF5 (IRF5-KO) and their WT littermates

treated for 2 or 24 h with LPS or palmitate (Palm) and epididymal white adipose tissue (EpiWAT) macrophages (ATMs) from IRF5-KO and WT mice following high-fat feeding for 4 or 12 weeks. Clustering analyses was applied to genes differentially expressed between genotypes in at least one condition. Normalised mRNA expression per cluster (left to right: LPS **** $p < 0.0001$, **** $p < 0.0001$, * $p = 0.028$, * $p = 0.031$, **** $p < 0.0001$, **** $p < 0.0001$; Palm ** $p = 0.016$, **** $p < 0.0001$, ** $p = 0.0038$, *** $p = 0.0003$, **** $p < 0.0001$, **** $p < 0.0001$; HFD * $p = 0.013$, ** $p = 0.0017$, * $p = 0.0156$, *** $p = 0.0001$; one-way ANOVA). C. Differential analysis between genotypes following 2- or 24-h treatment with LPS or Palm and in EpiWAT ATMs following 4 or 12 weeks of high-fat feeding ($\text{Log}_2\text{FC} > 1.0$; $-\text{Log}_{10}p > 1.3$). D. Venn diagram of differentially expressed genes between genotypes, per treatment condition. Percentage refers to proportion of genes in overlap. E. Gene track from ChIP-seq in A. of genes overlapping all conditions in F. also bound by IRF5. F. Correlative analyses of IRF5 expression and GHITM expression in BMDMs and ATMs from IRF5-competent mice. G. Mitochondrial cristae in electron micrograph and length and number of cristae of BMDMs from IRF5-KO and WT mice following Palm treatment for 2 h (* $p = 0.01$, * $p = 0.04$ unpaired t-test).

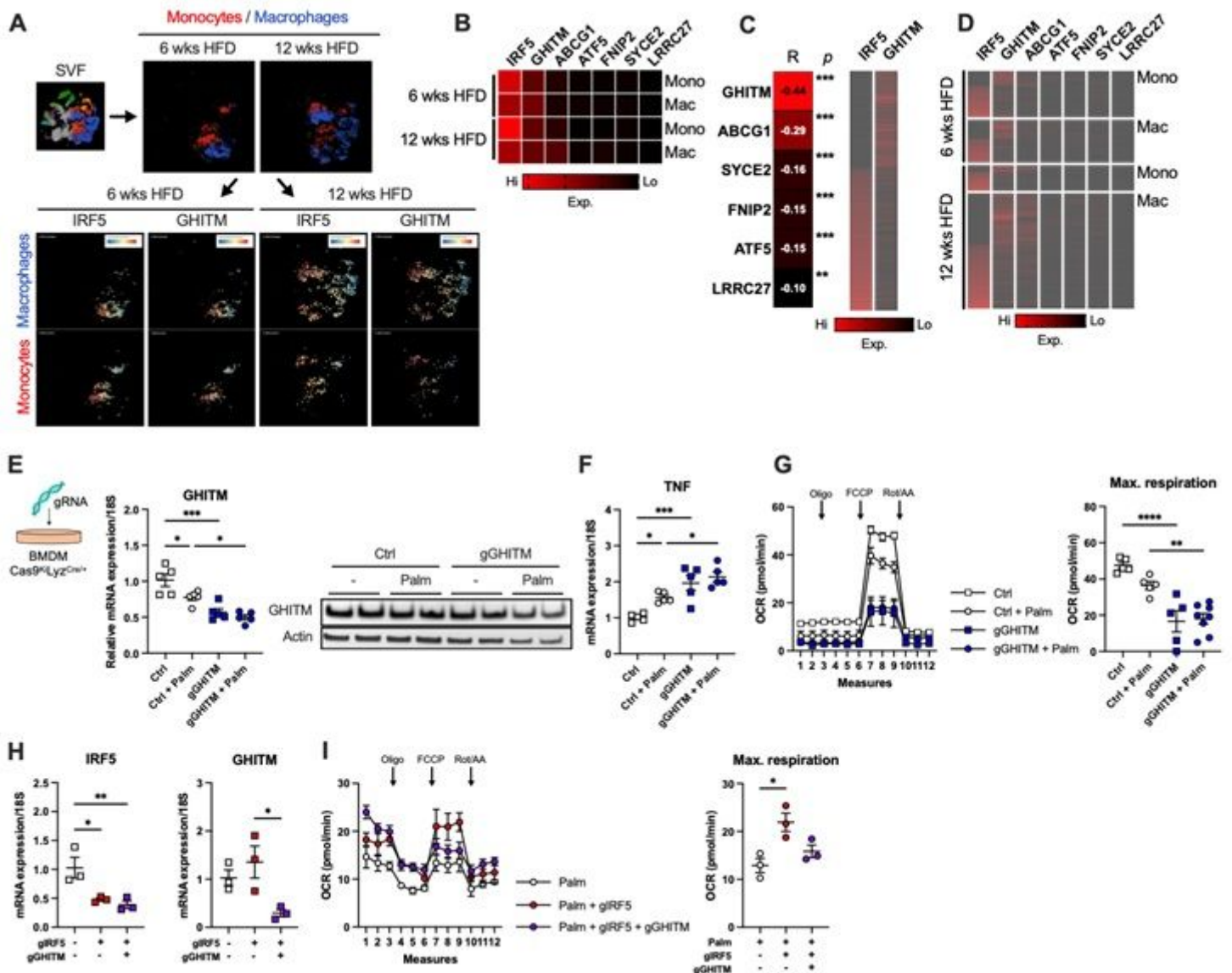


Figure 5

IRF5 and GHITM are highly expressed and reciprocally regulated in epididymal white adipose tissue macrophages and monocytes. A. Public dataset of single-cell RNA sequencing of the epididymal white adipose tissue stromal vascular fraction of C57BL/6J mice following 6 or 12 weeks of high-fat feeding. Macrophages and monocytes were identified and expression of IRF5 and of GHITM were projected onto tSNE plots per cell type and duration of high-fat feeding. B. Heatmap of mean expression values of IRF5, GHITM, ABCG1, SYCE2, FNIP2, ATF5 and LRRC27 over time and by cell type. C. Correlative analyses between IRF5 expression and expression of GHITM, ABCG1, SYCE2, FNIP2, ATF5 and LRRC27 at the single cell level (Pearson R; *** $p < 0.0001$ and ** $p = 0.004$). Heatmap of IRF5 and GHITM expression, each line represents a single cell. D. Heatmap of single cell expression of IRF5, GHITM, ABCG1, SYCE2, FNIP2, ATF5 and LRRC27 over time and by cell type, each line represents a single cell. E. Gene expression of GHITM in bone marrow-derived macrophages (BMDM) from mice with myeloid-restricted Cas9-GFP expression, treated with lipofection agent (Ctrl) or with a guide RNA (gRNA) targeting GHITM (gGHITM) and with or without Palm treatment for 2 h (n=5 per condition, one-way ANOVA. *** $p = 0.0003$, left * $p = 0.0423$, right * $p = 0.0167$). Western blotting against GHITM in the same experimental design, quantification in Fig. S4D (n=2 per condition). F. TNF mRNA expression in BMDMs as in E (*** $p = 0.0006$, left * $p = 0.04$, right * $p = 0.03$). G. Oxygen consumption rate (OCR) from mitochondrial stress test in BMDMs with or without Palm treatment following transfection with gGHITM or with lipofection agent alone (Ctrl). Oligomycin (Oligo), carbonyl cyanide 4-(trifluoromethoxy) phenylhydrazone (FCCP), rotenone/antimycin A (Rot/AA). Maximal respiration from mitochondrial stress test (n=5 for Ctrl, Ctrl + Palm and gGHITM; n=8 for gGHITM + Palm; one-way ANOVA, **** $p < 0.0001$ and ** $p = 0.0051$). H. Gene expression of IRF5 and GHITM in BMDMs following transfection with a gIRF5 gRNA or following double transfection with gGHITM and gIRF5 gRNAs or with lipofection agent alone (n=3 per condition; one-way ANOVA, * $p = 0.022$, ** $p = 0.009$ for IRF5; and * $p = 0.019$). I. OCR and maximal respiration from mitochondrial stress test on Palm treated BMDMs following transfection with a gRNA targeting IRF5 (gIRF5), double transfection with gGHITM and gIRF5 or with lipofection agent alone (Ctrl), (n=3 per condition; one-way ANOVA, * $p = 0.0428$).

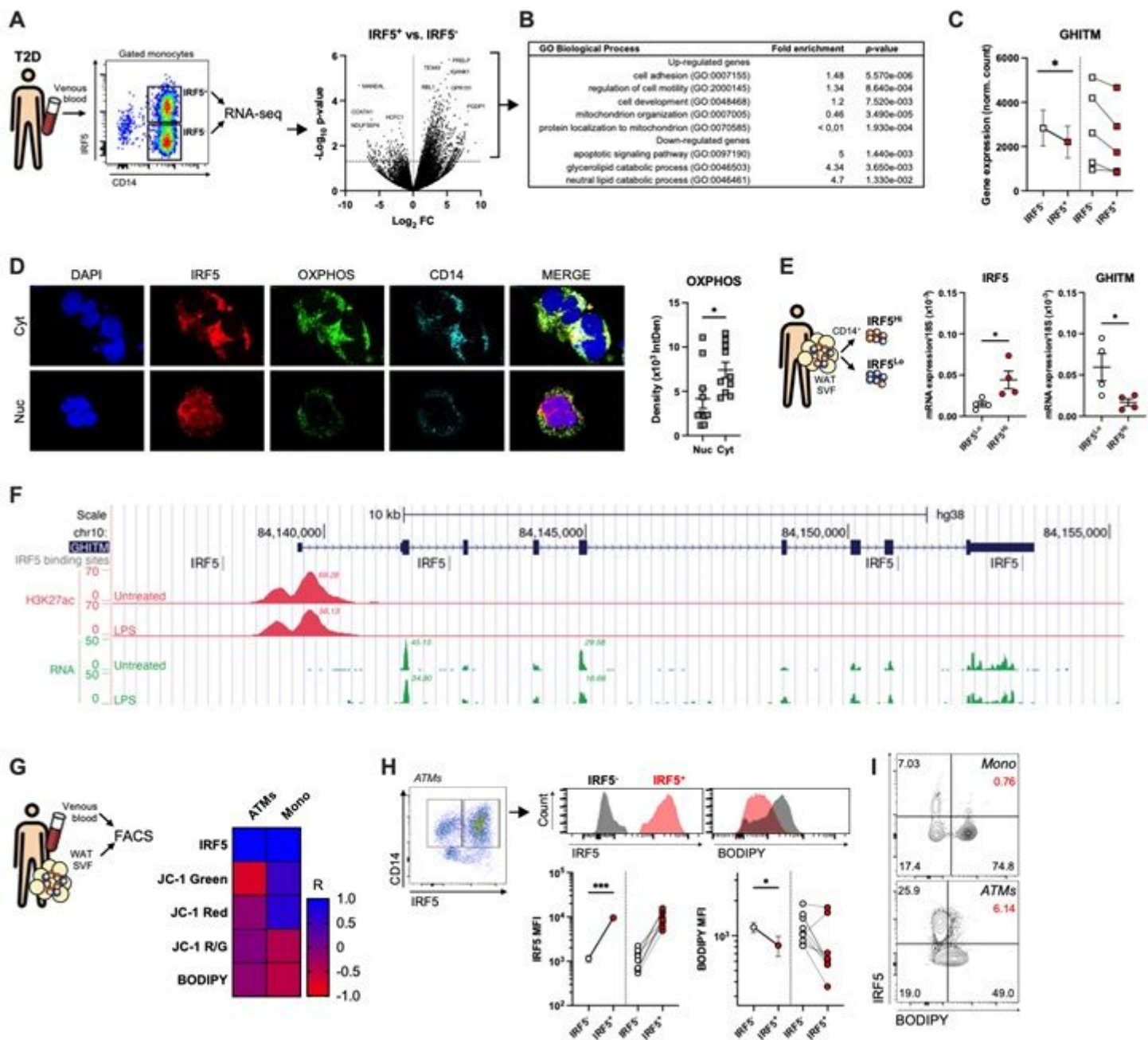


Figure 6

IRF5 binds to GHITM and regulates mitochondrial activity and cellular lipid content in human monocytes and adipose tissue macrophages. A. CD14⁺ Monocytes from patients with type-2 diabetes (T2D; n=5) were sorted based on their expression of IRF5 and subjected to RNA sequencing analyses. Differential analyses were paired by patient and carried out on IRF5⁺ versus IRF5⁻ monocytes (n=5, -log₁₀p>1.3). B. Gene ontology (GO) term enrichment analyses on up-regulated and down-regulated genes in IRF5⁺ versus IRF5⁻ monocytes. C. Expression of GHITM mRNA in IRF5⁻ and IRF5⁺ monocytes (*p=0.039, paired t-test). D. Immunofluorescence staining of IRF5, OXPPOS enzyme complexes and CD14 in cytospin prepared human monocytes from patients with T2D. Samples were separated based on IRF5 localisation being either nuclear (Nuc) or cytoplasmic (Cyt). Quantification of OXPPOS staining in IRF5 Nuc and Cyt samples (n=10 per condition, unpaired t-test, *p=0.0335) E. Expression of IRF5 and GHITM in CD14⁺

human adipose tissue macrophages (ATMs). Samples were stratified based on their expression level of IRF5 into IRF5Lo versus IRF5Hi expressers (n=4 per group, unpaired t-test, *p=0.039, *p=0.046). F. University of California Santa Cruz (UCSC) genome browser⁷²⁻⁷⁴ (<http://genome.ucsc.edu>) tracks at the GHITM locus with tracks from JASPAR202075 to visualize transcription factor binding sites for IRF5 and from BLUEPRINT^{76,77} to visualise RNA expression and H3K27 acetylation marks in LPS treated and untreated human monocyte-derived macrophages (session link). G. Correlative analyses of IRF5 expression, JC-1 green fluorescence, JC-1 red fluorescence, red-to-green fluorescence ratio and BODIPY fluorescence in human ATMs from obese patients and in monocytes from patients with T2D analysed by FACS (n=11 for monocytes, n=9 for ATMs, Pearson correlation). H. IRF5 expression and BODIPY fluorescence in IRF5+ and IRF5- ATMs (n=9 per group, ***p=0.0003, ****p<0.0001, *p=0.0195, two-way ANOVA). I. FACS quadrant plots of IRF5 expression and BODIPY fluorescence in ATMs and monocytes (Mono). Percentages in quadrants represent percentage of parent population.

Supplementary Files

This is a list of supplementary files associated with this preprint. Click to download.

- [SupplementaryMaterials.pdf](#)